

Numerical simulation of the von Kármán sodium dynamo experiment

C. Nore^{1,†}, D. Castanon Quiroz², L. Cappanera³ and J.-L. Guermond⁴

¹Laboratoire d'Informatique pour la Mécanique et les Sciences de l'Ingénieur, LIMSI, CNRS, Univ. Paris-Sud, Université Paris-Saclay, Bâtiment 508, rue John von Neumann, Campus Universitaire, F-91405 Orsay, France

²BCAM – Basque Center for Applied Mathematics, Mazarredo 14, E-48009 Bilbao, Basque Country, Spain

³Department of Computational and Applied Mathematics, Rice University, 6100 Main, MS-134, Houston, TX 77005, USA

⁴Department of Mathematics, Texas A&M University, 3368 TAMU, College Station, TX 77843-3368, USA

(Received 31 July 2017; revised 17 July 2018; accepted 20 July 2018;
first published online 3 September 2018)

We present hydrodynamic and magnetohydrodynamic (MHD) simulations of liquid sodium flows in the von Kármán sodium (VKS) set-up. The counter-rotating impellers made of soft iron that were used in the successful 2006 experiment are represented by means of a pseudo-penalty method. Hydrodynamic simulations are performed at high kinetic Reynolds numbers using a large eddy simulation technique. The results compare well with the experimental data: the flow is laminar and steady or slightly fluctuating at small angular frequencies; small scales fill the bulk and a Kolmogorov-like spectrum is obtained at large angular frequencies. Near the tips of the blades the flow is expelled and takes the form of intense helical vortices. The equatorial shear layer acquires a wavy shape due to three coherent co-rotating radial vortices as observed in hydrodynamic experiments. MHD computations are performed: at fixed kinetic Reynolds number, increasing the magnetic permeability of the impellers reduces the critical magnetic Reynolds number for dynamo action; at fixed magnetic permeability, increasing the kinetic Reynolds number also decreases the dynamo threshold. Our results support the conjecture that the critical magnetic Reynolds number tends to a constant as the kinetic Reynolds number tends to infinity. The resulting dynamo is a mostly axisymmetric axial dipole with an azimuthal component concentrated near the impellers as observed in the VKS experiment. A speculative mechanism for dynamo action in the VKS experiment is proposed.

Key words: dynamo theory, MHD and electrohydrodynamics

1. Introduction

Dynamo action, i.e. the self-amplification of a magnetic field by the flow of an electrically conducting fluid, is considered to be the main mechanism for the

† Email address for correspondence: caroline.nore@limsi.fr

generation of the magnetic fields of stars and planets (Moffatt 1978). In order to gain a better understanding of the processes at play, different experimental groups have investigated dynamo action (Peffley, Cawthorne & Lathrop 2000; Nornberg *et al.* 2006; Frick *et al.* 2010; Colgate *et al.* 2011) but so far only three experiments have been successful: Gailitis *et al.* (2000), Stieglitz & Müller (2001), Monchaux *et al.* (2007). These three experiments were all performed in liquid sodium. The first two experiments used optimized flows guided by pipes that intentionally limited the influence that turbulence could have on the dynamo process. The experimentalists found dynamo action with a magnetic field having a shape corresponding to the one predicted by using kinematic dynamo computations based on analytical flows. The third dynamo has been observed in the von Kármán sodium experiment (VKS) located in Cadarache: in 2006 experimentalists observed a magnetic field generated by a turbulent flow produced by two counter-rotating impellers in a cylindrical vessel. It has been found that both the geometry and the material composing the impellers play crucial roles in the dynamo action threshold: for example, at fixed available mechanical power, dynamo action occurs only when at least one of the rotating impellers is made of soft iron (Miralles *et al.* 2013). When the two soft iron impellers counter-rotate at the same angular velocity, another puzzling observation is that the generated magnetic field is statistically steady and mainly axisymmetric with an axial dipole and a strong azimuthal component located near the impellers (Boisson *et al.* 2012). This magnetic field could not be predicted by using simplified axisymmetric geometries and velocity fields averaged in azimuth and time: kinematic dynamo simulations usually give an equatorial dipole superimposed with two anti-parallel vertical magnetic structures near the vessel axis (see e.g. Ravelet *et al.* 2005, Laguerre *et al.* 2006, Marié, Normand & Daviaud 2006, Gissinger *et al.* 2008, Guermont *et al.* 2011a).

It is clear that the nature of the material composing the impellers greatly influences the transmission conditions enforced on the magnetic field, and that the geometry of the impellers controls the dynamics of the tip vortices generated between the blades (Ravelet *et al.* 2012; Kreuzahler *et al.* 2014). But a precise experimental investigation of the influences of the material properties and the blade geometry is not feasible due to the lack of accurate techniques such as non-intrusive Gaussmeters or PIV measurements in liquid metals. It is natural then to turn to computer simulations to gain some insight into the VKS experiment. The objective of the present work is to report on three-dimensional numerical simulations of the von Kármán sodium experiment at high kinetic Reynolds numbers. Dynamo action is obtained with a magnetic field that is mainly axisymmetric and similar to the one observed in the experiment. Some of these results were announced in Nore *et al.* (2016), but in the present paper we go well beyond the range of kinetic Reynolds numbers attained in the above reference. Our main result is that the critical magnetic Reynolds number decreases as the kinetic Reynolds number increases and this number seems to converge to a constant at very large kinetic Reynolds numbers. We also confirm that, everything else being fixed, the critical magnetic Reynolds number decreases as the magnetic permeability of the impellers increases.

The paper is organized as follows. The set-up of the 2006 VKS2 experiment together with the relevant parameters is shortly presented in §2. The governing equations and the numerical methods that are used to solve them are also briefly described. Section 3 presents hydrodynamical simulations performed for a large range of kinetic Reynolds numbers. Dynamo action is studied in §4. The impact of the relative magnetic permeability of the impellers and of the boundary conditions is

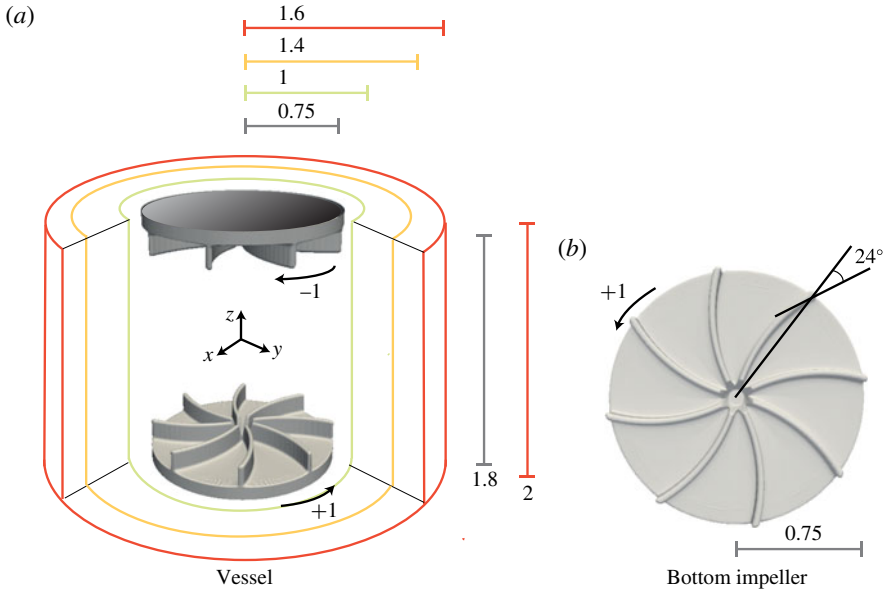


FIGURE 1. (Colour online) Schematic of the VKS2 experimental device of Monchaux *et al.* (2007) in non-dimensional units. The impellers counter-rotate as indicated in (a) and are fitted with eight curved blades (b).

studied. The dynamo threshold is determined for a large range of kinetic Reynolds numbers; it decreases as the kinetic Reynolds number increases and it seems to reach an asymptotic value for very large kinetic Reynolds numbers. The structure of the generated magnetic field shows a striking similarity with the one observed in the VKS2 experiment in all of the cases investigated. Key ingredients for dynamo action in the VKS2 set-up are identified in § 5. It is shown in particular in this section that kinematic dynamo computations using the time-averaged velocity field computed at high fluid Reynolds number give a non-axisymmetric magnetic field similar to the one obtained from simplified time-averaged and azimuthally averaged velocity field, but this dynamo is very different from the one observed in VKS2 experiment. Concluding remarks are reported in § 6 and a tentative scenario is proposed.

2. Technical preliminaries

In the present paper we simulate numerically the VKS2 experiment with the flow driven by the TM73 impellers (see figure 1 and Monchaux *et al.* (2007)). We begin by describing the geometry. Then we present the governing equations and the algorithms that are used in our magnetohydrodynamic (MHD) code (Guermond *et al.* 2007, 2009, 2011a).

2.1. Experimental set-up and data

The VKS2 set-up described in Monchaux *et al.* (2007) uses two concentric cylindrical containers: the first one has a very small thickness and is of radius $R_{cyl} = 206$ mm; the second one is thick and made of copper, its inner radius is $R_{in} = 289$ mm and its outer radius is $R_{out} = 330$ mm. Both containers have a total height $H = 412$ mm. The

impellers are located at the two extremities of the inner container. There is some fluid behind the impellers in the experiment, but in the present simulations we neglect this fluid layer. The impellers are composed of two disks each supporting eight blades. The disks have radius $R_b = 155$ mm and are 20 mm thick. The blades have height 41 mm, thickness 5 mm, and the angle of curvature is equal to 24° . The distance between the inner faces of the disks is set to 370 mm so that the aspect ratio of the cylindrical fluid domain is $370/206 = 1.8$. The fluid contained in the inner vessel is pushed by the convex side of the blades. A schematic representation of the experimental set-up is shown in figure 1 using R_{cyl} as reference length scale.

The vessel contains approximately 150 l of liquid sodium heated at 120°C . The kinematic viscosity is $\nu = 6.78 \times 10^{-7}$ m² s⁻¹, the density is $\rho = 932$ kg m⁻³ and the electrical conductivity is $\sigma = 9.6 \times 10^6$ S m⁻¹. The corresponding magnetic Prandtl number is $P_m = \mu_0 \sigma \nu = 0.82 \times 10^{-5}$. The impellers counter-rotate at a frequency f , the experimental range of frequencies necessary for observing dynamo action is $16 \text{ Hz} \leq f \leq 22 \text{ Hz}$, leading to kinetic Reynolds numbers in the range $6.3 \times 10^6 \leq Re = 2\pi f R_{cyl}^2 / \nu \leq 8.7 \times 10^6$ and magnetic Reynolds numbers in the range $52 \leq R_m^c = \mu_0 \sigma 2\pi f R_{cyl}^2 \leq 71$.

At maximum available mechanical power, a dynamo has been observed with soft iron impellers (made of ferromagnetic material of relative magnetic permeability of the order of 50, see Verhille *et al.* (2010)) but not with stainless steel ones (Miralles *et al.* 2013).

2.2. Spectral/finite element code for Maxwell and Navier–Stokes equations (SFEMaNS)

To investigate the hydrodynamic and magnetohydrodynamic regimes of the above experimental set-up, we use a code henceforth referred to in this paper as SFEMaNS. This code uses a hybrid spatial discretization combining spectral and finite elements. In a nutshell the code uses a Fourier decomposition in the azimuthal direction and the continuous Hood–Taylor Lagrange elements $\mathbb{P}_1\text{--}\mathbb{P}_2$ for the pressure and velocity fields in the meridian section. Modulo the computations of nonlinear terms with the fast Fourier transform (FFT), the linear problems for each Fourier mode in the meridian section are uncoupled and are thereby easily parallelized by using the message passing interface (MPI). The solution of the linear problems in the meridian section is further parallelized by using graph partitioning techniques from the METIS library (Karypis & Kumar 1998) for the domain decomposition, and subroutines from the portable extensible toolkit for scientific computation library (PETSc) (Balay *et al.* 2014) for the linear algebra. For the magnetic part, the algorithm solves the problem using the magnetic induction, \mathbf{B} , in the conducting region (after standard elimination of the electric field) and the scalar magnetic potential in the insulating exterior. The fields in each region are approximated by using H^1 -conforming Lagrange elements with a penalty technique to control the divergence of \mathbf{B} in a negative Sobolev norm that guarantees convergence under minimal regularity (see details in Giesecke *et al.* (2010, §3.2), Bonito & Guermond (2011), Bonito, Guermond & Luddens (2013)). The coupling between conducting and insulating media is done by using an interior penalty method. SFEMaNS has been thoroughly validated on numerous manufactured solutions and against other MHD codes (see e.g. Guermond *et al.* 2009; Giesecke *et al.* 2012; Nore *et al.* 2016). The reader who is familiar with the numerical details or is not interested in such details is now invited to jump to § 3.

2.3. Governing equations

Let us now go into some details about the equations that are actually solved in SFEMaNS. The MHD equations are solved in non-dimensional form as follows:

$$\partial_t \mathbf{u} = -(\nabla \times \mathbf{u}) \times \mathbf{u} + \frac{1}{R_e} \Delta \mathbf{u} - \nabla p + \mathbf{f}, \quad (2.1a)$$

$$\partial_t \mathbf{B} = \nabla \times (\mathbf{u} \times \mathbf{B}) - \frac{1}{R_m} \nabla \times \left(\frac{1}{\sigma_r} \nabla \times \left(\frac{1}{\mu_r} \mathbf{B} \right) \right), \quad (2.1b)$$

$$\nabla \cdot \mathbf{u} = 0, \quad (2.1c)$$

$$\nabla \cdot \mathbf{B} = 0, \quad (2.1d)$$

where \mathbf{u} is the velocity field, \mathbf{B} the magnetic induction field (with the magnetic field $\mathbf{H} = \mathbf{B}/\mu_0\mu_r$), p the pressure field and σ_r , μ_r are the relative conductivity and permeability of the various materials present. The Navier–Stokes and the Maxwell equations are coupled by the Lorentz force $\mathbf{f} = (\nabla \times \mathbf{H}) \times \mathbf{B}$.

In the present situation the reference length L_{ref} is set to R_{cyl} . The computational domain for the hydrodynamic study is $\Omega = \{(r, \theta, z) \in [0, 1] \times [0, 2\pi] \times [-1, 1]\}$. The computational domain for the MHD study is the larger cylinder $\Omega \cup \Omega_{out}$ with $\Omega_{out} = \{(r, \theta, z) \in [1, 1.6] \times [0, 2\pi] \times [-1, 1]\}$ (the geometric dimensions and sketches of the set-up are shown in figures 6c and 19b). Denoting by σ_0 the electrical conductivity of the liquid sodium, ρ its density and μ_0 the magnetic permeability of vacuum, the magnetic induction is made non-dimensional by using the Alfvén scaling $\mathbf{B} = U\sqrt{\rho\mu_0}$, with $U = \omega R_{cyl}$ where ω is the angular velocity of the impellers. The two governing parameters are $R_m = \mu_0\sigma_0 R_{cyl}^2\omega$, the magnetic Reynolds number, and $R_e = R_{cyl}^2\omega/\nu$, the kinetic Reynolds number, with ν the kinematic viscosity of the fluid.

Note that the parameters σ_r , μ_r are not constant since the walls and the impellers are made of different materials such as copper, steel and soft iron. Specifically, we take $\sigma_r = 1$, $\mu_r = 1$ in the region $\{(r, \theta, z) \in [1, 1.4] \times [0, 2\pi] \times [-1, 1]\}$ to represent the lateral layer of stagnant liquid sodium, and $\sigma_r = 4.5$, $\mu_r = 1$ in $\{(r, \theta, z) \in [1.4, 1.6] \times [0, 2\pi] \times [-1, 1]\}$ to model the lateral copper wall. The computational domain is slightly smaller than the actual VKS2 container: it does not contain the so-called lid layers, which have been shown in kinematic dynamo simulations to be detrimental to dynamo action, Stefani *et al.* (2006), Laguerre *et al.* (2006). In the induction equation (2.1b) we take $\mathbf{u}|_{\Omega_{out}} = 0$. With the exception of § 4.3 where we study the impact of the so-called vacuum boundary condition, in the entire paper we impose the perfect ferromagnetic boundary condition $\mathbf{H} \times \mathbf{n} = 0$ at the boundary of the computational domain. We shall also refer to this condition as the pseudo-vacuum boundary condition. This boundary condition allows us to save memory and CPU time.

2.4. Moving domains

To distinguish the liquid sodium from the impellers, the cylinder Ω is split into a solid domain $\Omega_{solid}(t)$ (composed of the rotating impellers) and a fluid domain $\Omega_{fluid}(t)$, and we introduce the characteristic function χ defined in cylindrical coordinates by:

$$\chi(r, \theta, z, t) = \begin{cases} 1 & \text{if } (r, \theta, z) \in \Omega_{fluid}(t), \\ 0 & \text{if } (r, \theta, z) \in \Omega_{solid}(t). \end{cases} \quad (2.2)$$

In our case $\chi = 0$ in the impellers (see figure 1). Note that both $\Omega_{solid}(t)$ and $\Omega_{fluid}(t)$ are time dependent. It is not possible to find a frame of reference where these domains

are time independent since the impellers move with opposite angular velocities. The ensuing main difficulty is to approximate the Navier–Stokes equations in a time- and θ -dependent domain and to force the velocity in the solid domain $\Omega_{solid}(t)$ to be that of two solid bodies in rotation. This is achieved by using a prediction–correction method of Guermond & Shen (2004) and a pseudo-penalty technique of Pasquetti, Bwemba & Cousin (2008). Let τ be the time step and let us generically denote by f^n the approximation of $f(n\tau)$. The velocity is then updated by using the following scheme:

$$\frac{3\mathbf{u}^{n+1}}{2\tau} - \frac{1}{R_e}\Delta\mathbf{u}^{n+1} = -\nabla p^n + (1 - \chi^{n+1})\frac{3\mathbf{u}_{obs}^{n+1}}{2\tau} + \chi^{n+1}\left(\frac{4\mathbf{u}^n - \mathbf{u}^{n-1}}{2\tau} - \nabla\left(\frac{4\psi^n - \psi^{n-1}}{3}\right) - (\nabla \times \mathbf{u}^{*,n+1}) \times \mathbf{u}^{*,n+1} + \mathbf{f}^{n+1}\right), \quad (2.3)$$

where $\mathbf{u}^{*,n+1} = 2\mathbf{u}^n - \mathbf{u}^{n-1}$ and, using cylindrical coordinates, \mathbf{u}_{obs} is the velocity of the disks and blades defined for all $n \geq 0$ by:

$$\mathbf{u}_{obs}^n(r, \theta, z) = \begin{cases} -r\mathbf{e}_\theta & \text{if } z > 0, \\ r\mathbf{e}_\theta & \text{if } z \leq 0. \end{cases} \quad (2.4)$$

The pressure increment ψ^{n+1} is obtained by solving the following Poisson problem:

$$\Delta\psi^{n+1} = \frac{3}{2\tau}\nabla \cdot \mathbf{u}^{n+1}. \quad (2.5)$$

The pressure is finally updated as follows:

$$p^{n+1} = p^n + \psi^{n+1} - \frac{1}{R_e}\nabla \cdot \mathbf{u}^{n+1}. \quad (2.6)$$

Note that the velocity and the pressure are solutions of the Navier–Stokes equations when $\chi = 1$, i.e. in the fluid domain $\Omega_{fluid}(t)$. When $\chi = 0$, i.e. in $\Omega_{solid}(t)$, the momentum equation reduces to $3\mathbf{u}^{n+1}/2\tau - (1/R_e)\Delta\mathbf{u}^{n+1} = -\nabla p^n + 3\mathbf{u}_{obs}^{n+1}/2\tau$; to first order in τ , the solution is $\mathbf{u} = \mathbf{u}_{obs} + O(\tau/R_e)$. Note that the higher the kinetic Reynolds number, the more accurate the method. There are two situations for the initialization of the above algorithm. Either we start from rest, and in this case all the quantities required at $n = 0$ are set to zero, or we restart from a previous computation, and in this case all the quantities required to restart are taken from the previous computation.

The second difficulty we face is that the material properties in the computational frame depend on the azimuthal angle and time due to the presence of the rotating blades. This is not a serious issue for the conductivity σ_r since the conductivity of the impellers and the liquid sodium are not very different; for the sake of simplicity we take $\sigma_r = 1$ in the impellers and in the liquid sodium. But to account for the heterogeneities of the magnetic permeability, we allow μ_r to depend on all the space and time variables, i.e. $\mu_r = \mu_r(r, \theta, z, t)$. More precisely, letting μ_r^{imp} be the relative permeability of the impellers and recalling that $\mu_r = 1$ in the liquid sodium, we set

$$\mu_r(r, \theta, z, t) = \chi(r, \theta, z, t) + (1 - \chi(r, \theta, z, t))\mu_r^{imp}. \quad (2.7)$$

In order to make the linear algebra in the induction equation time independent, and to avoid the nonlinearity in θ induced by the product $(1/\mu_r)\mathbf{B}$, we split the diffusion

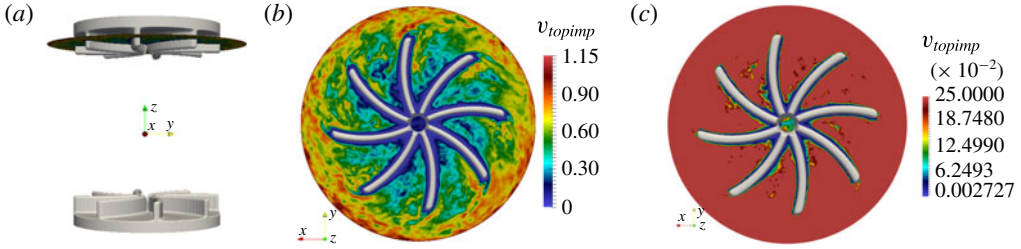


FIGURE 2. (Colour online) Velocity field in the reference frame of the top impeller at $R_e = 10^5$ and isovalues of the function χ . (a) Isovalue $\chi = 0.75$ inside the blades and the cutting plane at $z = 0.8$; (b) isovalue $\chi = 0.75$ and $\|\mathbf{u} - \mathbf{u}_{top-impeller}\|$ in the plane $z = 0.8$ seen from below; (c) isovalue $\chi = 0.925$ and $\|\mathbf{u} - \mathbf{u}_{top-impeller}\|$ (partial scale between 0 and 0.25).

term by setting $\mathbf{B}/\mu_r = \mathbf{B}/\widetilde{\mu}_r + (\mathbf{B}/\mu_r - \mathbf{B}/\widetilde{\mu}_r)$, where $\widetilde{\mu}_r(r, z)$ is defined by $\widetilde{\mu}_r(r, z) := \min_{0 \leq \theta < 2\pi} \mu_r(r, \theta, z, t)$. The first part of the decomposition, $\mathbf{B}/\widetilde{\mu}_r$, is made implicit while the second part, $(\mathbf{B}/\mu_r - \mathbf{B}/\widetilde{\mu}_r)$, is made explicit by using $\mathbf{B}^{*,n+1} = 2\mathbf{B}^n - \mathbf{B}^{n-1}$ and $\mu_r = \mu_r^{n+1}$. The magnetic induction field is therefore updated as follows:

$$\frac{3\mathbf{B}^{n+1}}{2\tau} + \frac{1}{R_m} \nabla \times \left(\frac{1}{\sigma_r} \nabla \times \left(\frac{\mathbf{B}^{n+1}}{\widetilde{\mu}_r} \right) \right) = \frac{4\mathbf{B}^n - \mathbf{B}^{n-1}}{2\tau} + \nabla \times (\mathbf{u}^{n+1} \times \mathbf{B}^{*,n+1}) - \frac{1}{R_m} \nabla \times \left(\frac{1}{\sigma_r} \nabla \times \left(\mathbf{B}^{*,n+1} \left(\frac{1}{\mu_r} - \frac{1}{\widetilde{\mu}_r} \right) \right) \right). \quad (2.8)$$

The function $\widetilde{\mu}_r$ being independent of the azimuth, implicit FFT convolutions are completely avoided. Note also that for each Fourier mode, the linear problem in (2.8) is decoupled from the other Fourier modes. The scheme (2.8) is stable, owing to the condition $\widetilde{\mu}_r \leq \mu_r$, and it can be shown to be second-order accurate in time, see Castanon Quiroz (2015) for details. Finally, the solenoidal constraint (2.1d) is enforced as in Guermond *et al.* (2011a).

To illustrate the performance of the penalty method, we show in figure 2 some isovalues of the function χ and the amplitude of the velocity field in the reference frame of the top impeller at some arbitrary time at $R_e = 10^5$. Figure 2(a) shows the isovalue $\chi = 0.75$ in grey and the cutting plane at $z = 0.8$. The actual boundary of the blades corresponds to $\chi = 0.99$; therefore, the isovalue $\chi = 0.75$ is inside the blades. Figure 2(b) shows $\|\mathbf{u} - \mathbf{u}_{top-impeller}\|$ in the plane $z = 0.8$ seen from below. The relative velocity is nearly zero in the blades. To emphasize the velocity gradient close to the blades, we show in figure 2(c) the amplitude of the relative velocity in the range $[0, 0.25]$ and the isovalue $\chi = 0.925$. The red colour indicates values well above 0.25 in the bulk of the fluid. The boundary layer around the blade is visible in blue. Close to the isocontour $\chi = 0.925$, the amplitude of the relative velocity is smaller than 0.02; hence the relative value of the relative velocity is definitely smaller than 1.7% within the blades. This value is significantly smaller in the region $\chi < 0.75$. These results confirm that the pseudo-penalty technique performs as expected.

2.5. Entropy viscosity stabilization

When R_e is moderate, it is possible to resolve all the scales by refining the grid and by enriching the Fourier space, i.e. it is possible to perform direct numerical

simulations (DNS, see table 1), but, given that computer resources are finite, this is no longer feasible when R_e becomes large. More specifically, given a fixed computational budget, large gradients induced by the turbulence cascade can no longer be correctly represented numerically for Reynolds numbers beyond a few thousands. The energy that should have been dissipated at the Kolmogorov scale accumulates at the grid scale. A stabilization method that handles this problem has been implemented in SFEMaNS. This method, called entropy viscosity, and denoted LES in table 1, was developed in Guermond, Marra & Quartapelle (2006), Guermond, Pasquetti & Popov (2011*b*) and Guermond, Pasquetti & Popov (2011*c*). It consists of adding a local artificial viscosity made proportional to the residual of the kinetic energy balance. This artificial viscosity is added on the right-hand side of (2.1*a*) in the form $\nabla \cdot (\nu_E \nabla \mathbf{u})$. This induces a nonlinear diffusion proportional to the local energy imbalance that in turn allows the unresolved scales to be better accounted for. The method has its roots in the notion of suitable weak solutions introduced by Scheffer (1987) and has been shown by Caffarelli, Kohn & Nirenberg (1982) to be the only reasonable notion of solution currently available for the three-dimensional Navier–Stokes equations.

Let us now give some technical details on the computation of the entropy viscosity. We consider a mesh \mathcal{K}_h of the computational domain composed of a collection of three-dimensional cells K . Since in the present situation the approximation mixes finite elements and Fourier approximation, the mesh \mathcal{K}_h in question is the tensor product of the finite element mesh in the meridian section and the uniform azimuthal one-dimensional mesh induced by the Fourier approximation. Denoting by M the number of complex azimuthal Fourier modes, the mesh size in the azimuthal direct at the radius r is $2\pi r/(2M - 1)$. We denote by h_K the minimum of $2\pi r/(2M - 1)$ over K and the diameter of the corresponding finite element cell, and we refer to h_K as being the size of K . Assuming that $n \geq 2$ (or \mathbf{u}^{-2} , \mathbf{u}^{-1} and p^{-1} have been initialized appropriately), we define the residual of the momentum equation as follows:

$$\text{Res}_{NS}^n = \frac{\mathbf{u}^n - \mathbf{u}^{n-2}}{2\tau} + (\mathbf{u}^{n-1} \cdot \nabla) \mathbf{u}^{n-1} - \frac{1}{R_e} \Delta \mathbf{u}^{n-1} + \nabla p^{n-1} - \mathbf{f}^{n-1}. \tag{2.9}$$

This residual is computed at each time step and over every mesh cell in the real space. The local artificial viscosity is defined on each cell K by:

$$\nu_{R|K}^n = \frac{h_K^2 \|\text{Res}_{NS}^n \cdot \mathbf{u}^n\|_{L^\infty(D_K)}}{\|\mathbf{u}^n\|_{L^\infty(D_K)}^2}, \tag{2.10}$$

where D_K is the patch composed of the cells sharing one face with the cell K in the real space. The quantity $\nu_{R|K}^n$ is expected to be as small as the consistency error in smooth regions and to be large in the regions where the Navier–Stokes equations are not resolved well. To be able to run with Courant–Friedrichs–Lewy (CFL) numbers of order $O(1)$, we finally define the entropy viscosity as follows:

$$\nu_{E|K}^n = \min(c_{max} h_K \|\mathbf{u}^n\|_{L^\infty(D_K)}, c_e \nu_{R|K}^n), \tag{2.11}$$

where $c_{max} = 1/8$ (for \mathbb{P}_2 approximation on the velocity) and c_e is a tuneable constant $O(1)$. Thus defined, and given that we use \mathbb{P}_2 polynomials to approximate the velocity, the entropy viscosity scales like $O(h_K^3)$ in smooth regions and scales like $O(h_K)$ in regions with very large gradients.

Let us finish this section by mentioning that in all the MHD computations reported in the paper no artificial viscosity was added in the induction equation (2.1*b*). Since

R_e	1.5×10^3	1.5×10^3	1.5×10^3	2.5×10^3	10^4	10^5
R_m	[50, 300]	[50, 300]	[50, 300]	[50, 150]	[50, 150]	[50, 100]
Model	DNS	—	—	LES	—	—
μ_r^{imp}	1	5	50	50	50	50
τ	1.25×10^{-3}	1.25×10^{-3}	10^{-3}	10^{-3}	1.25×10^{-3}	1.25×10^{-3}
h_{min}	2.5×10^{-3}	—	—	5×10^{-3}	—	—
h_{max}	10^{-2}	—	—	—	—	—
modes	128	128	128	144	168 or 256	168 or 256
nprocs	64	64	192	360	336 or 512	336 or 512

TABLE 1. Numerical parameters for the MHD computations: kinetic Reynolds number R_e , magnetic Reynolds number R_m , numerical model DNS or LES, maximum relative magnetic permeability for impellers μ_r^{imp} , time step, mesh size in the blade region h_{min} , mesh size at the outer boundary h_{max} (the meridian mesh is non-uniform), number of real Fourier modes, number of processors.

the magnetic Reynolds number R_m is always far smaller than the kinetic Reynolds number, the magnetic field is always correctly represented by the finite element mesh, i.e. equation (2.1b) is always solved with DNS, and, depending on the value of R_e , equation (2.3) is solved with DNS or LES. Which method is used will be stated in all the cases.

2.6. Summary of the numerical parameters

The numerical parameters that have been used in the various simulations reported in the paper are listed in table 1. The spatial resolution of a typical DNS run in the meridian plane is $h_{min} = 2.5 \times 10^{-3}$ in the blade region and $h_{max} = 10^{-2}$ close to the outer boundary and slightly coarser for a typical LES run. Using that the thickness of the boundary layer on the blades is given by $\delta_{BL}/R_{cyl} = O(1/\sqrt{R_e})$, we estimate that there is only one grid point in the viscous boundary layer; notice though that the magnetic boundary layer is always well resolved since $R_m \in [50, 300]$. Although the viscous layer is under-resolved, we have verified by making comparisons with experiments in the range $R_e \in [10^2, 10^5]$ (Ravelet, Chiffaudel & Daviaud 2008, figure 7), that the code computes accurately the torque applied by the blades to the fluid (tests not reported here). Between 128 and 256 real Fourier modes are used. The parallelization is done with one complex Fourier mode per processor, and the meridian plane is further divided among the processors by using a domain decomposition technique, the graph partitioning being done by METIS. The linear algebra in the meridian section is handled by PETSc and the FFTs are done with FFT3W. One rotation period (one turn) requires between five and eight wall-clock hours on a medium capacity parallel machine called Brazos at Texas A&M University with quad core Intel Xeon, AMD Opteron and 8-core AMD Opteron, and it takes between two and four wall-clock hours on the cluster IBM x3750-M4 from GENCI-IDRIS. Each run does between 15 and 60 turns. The cumulated computing time for the runs presented in this article is approximately 5×10^5 CPU hours on one processor.

3. Hydrodynamic study

We first perform hydrodynamic computations by solving (2.1a)–(2.1c) with R_e in the range $\{2 \times 10^2, 5 \times 10^2, 10^3, 1.5 \times 10^3, 2.5 \times 10^3, 5 \times 10^3, 10^4, 10^5\}$. We characterize the structures of the flow through three-dimensional visualizations and

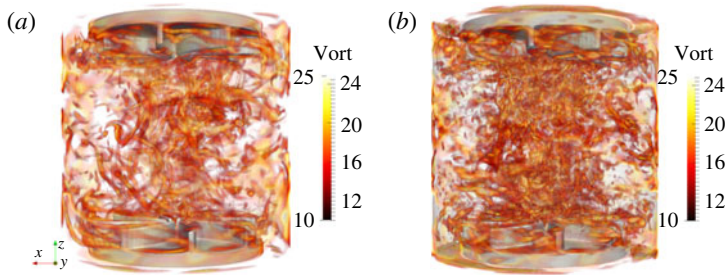


FIGURE 3. (Colour online) Navier–Stokes simulations in the TM73 VKS2 configuration in the cylinder of radius $r = 1$: (a) at $Re = 10^4$, partial scale for the amplitude of the vorticity field, $\|\nabla \times \mathbf{u}\|$ (between 10 and 25 for a total scale between 0 and 56) and (b) at $Re = 10^5$ partial scale for the amplitude of the vorticity field, $\|\nabla \times \mathbf{u}\|$ (between 10 and 25 for a total scale between 0 and 99). The impellers are represented in light grey.

by computing various time-averaged physical quantities. The visualizations, the global quantities and the spatial spectra are in agreement with the experimental observations and the Kolmogorov scenario. All the simulations done at $Re = 5 \times 10^3$ and beyond have been done with the entropy viscosity technique presented previously.

3.1. Turbulent flow at high Reynolds numbers

We start by investigating the qualitative behaviour of the flow at high Reynolds numbers. Figure 3 shows snapshots of the vorticity field at $Re = 10^4$ and $Re = 10^5$ characterized by small-scale structures with a clustering near the symmetry axis. The numerous vorticity tubes are characteristic of fully developed turbulence. Elongated vortical structures are attached to the concave side of the impeller blades.

We show in figure 4 one snapshot of the velocity field computed at $Re = 10^5$. The flow is clearly turbulent as small scales have invaded the entire fluid domain. In the yOz plane the velocity components $\{u_x, u_y\}$ show ejection motions near the tip of the impellers. Close to the symmetry axis, the u_z -component shows strong axial motions that are oriented toward the impellers and which are characteristics of the Ekman suction induced by them (see figure 4*a–c*). The representation of the velocity vector field on the cylindrical surface $\{r = 0.8\}$ reveals two counter-rotating zonal flows at the top and bottom of the vessel which are induced by the impellers. We also observe large-scale structures in the equatorial plane where the $\{u_\theta, u_z\}$ -components are significantly larger than the radial component u_r (see figure 4*d,e*).

The overall structure is made more visible by inspecting the time average of the velocity field (see figure 5*a–g*). We observe two counter-rotating recirculation tori separated by an active azimuthal shear layer localized at the equator. Kinetic energy is injected by the impellers, the flow spirals up or down along the side wall and is driven radially inward at mid-plane. The two resulting inward flows meet at the equator and form a shear layer that dissipates energy. Note that the components of the time-averaged velocity shown in figure 5*(a–c)* are not fully symmetric with respect to the Oz and Oy axes due to the presence of the azimuthal Fourier mode $m = 3$. The spectra reported in figure 10 show that the azimuthal Fourier mode $m = 3$ is persistent over a wide range of Reynolds numbers. This energy peak at $m = 3$ corresponds to three radial co-rotating vortices seen in figure 5*(d,e)*. These cat's-eye structures are the manifestation of the Kelvin–Helmholtz instability of the equatorial shear layer (Nore *et al.* 2003). These vortices are localized near the equator and form a complex three-dimensional structure inside the bulk, as evidenced in figure 5*(f,g)*. Similar cat's-eye

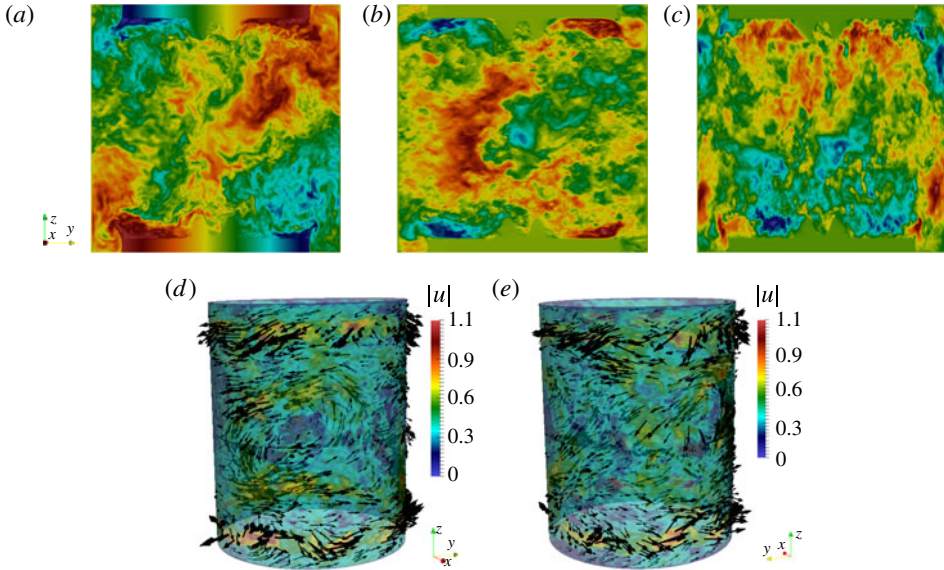


FIGURE 4. (Colour online) Navier–Stokes simulations in the TM73 VKS2 configuration at $R_e = 10^5$. Snapshots of the velocity field in the plane yOz ($-1 \leq y \leq 1$, $-1 \leq z \leq 1$): (a) u_x (scale between -0.94 (blue) and 0.85 (red)); (b) u_y (scale between -0.83 (blue) and 0.77 (red)); (c) u_z (scale between -0.66 (blue) and 0.69 (red)). Snapshots of the velocity vector field on the cylindrical surface $\{r=0.8\}$: (d) for $-\pi/2 \leq \theta \leq \pi/2$; (e) for $\pi/2 \leq \theta \leq 3\pi/2$.

vortices have been experimentally observed by Cortet *et al.* (2009) at very high Reynolds numbers. It is reported therein that ‘these vortices fluctuate in azimuthal position as well as in amplitude or apparent size’. The fact that these structures are visible in our time average may be due to the Reynolds number not being large enough or the range of the time averaging being too short.

As seen in figure 6(a), the global kinetic helicity $\text{Hel}_K(t) := \int_{\Omega} \mathbf{u}(\mathbf{r}, t) \cdot \nabla \times \mathbf{u}(\mathbf{r}, t) \, d\Omega$ is negative during the entire time of evolution. This is not a surprise since the Ekman suction creates a strong vertical velocity field moving toward each impeller and the product of this velocity field with the angular velocity of the impellers is predominantly negative. However, the spatial distribution of the local helicity $\mathbf{u}(\mathbf{r}, t) \cdot \nabla \times \mathbf{u}(\mathbf{r}, t)$ is complex and exhibits fine scales (see figure 6(b,c)). The maxima are always localized near the impellers whereas the minima are dispersed over the whole fluid domain. This is well illustrated in figure 6(c) where we show the helicity field of the time-averaged velocity. As first numerically evidenced by Ravelet *et al.* (2012), Kreuzahler *et al.* (2014) and seen in figure 3, the positive maxima are associated with the swirling vortices attached to each blade and occupying part of the space between the blades. These vortices are thought to be a key ingredient of the dynamo mechanism (Laguerre *et al.* 2008; Gissinger 2009; Varela *et al.* 2015).

3.2. Global quantities

We now make quantitative diagnostics to get a better understanding of the dynamics. Given a finite time series f^1, \dots, f^q , we define the time average \bar{f} as follows:

$$\bar{f} := \frac{1}{q} \sum_{1 \leq n \leq q} f^n. \quad (3.1)$$

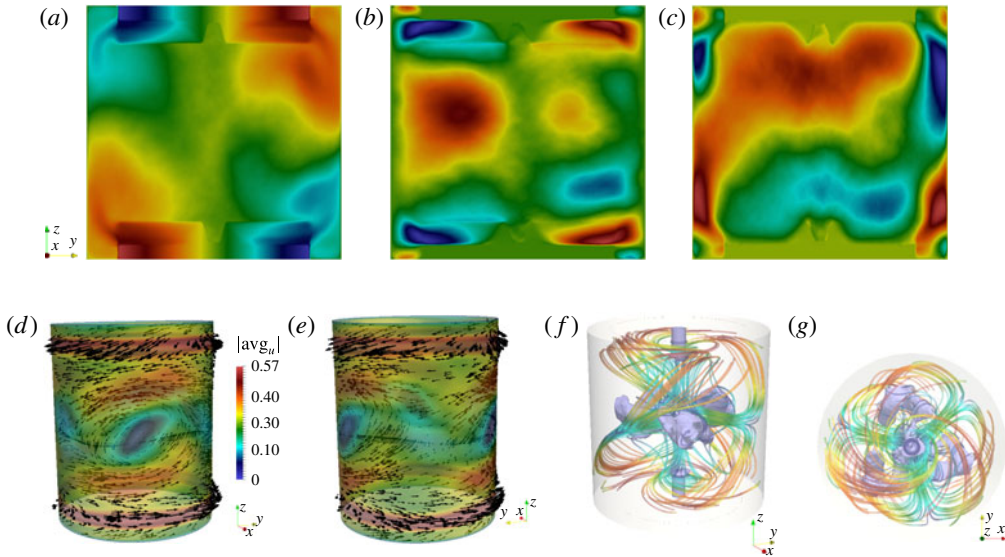


FIGURE 5. (Colour online) Time-averaged velocity field in Navier–Stokes simulations for the TM73 VKS2 configuration at $Re = 10^5$. Velocity field in the plane yOz ($-1 \leq y \leq 1$, $-1 \leq z \leq 1$): (a) \bar{u}_x (scale between -0.75 (blue) and 0.75 (red)); (b) \bar{u}_y (scale between -0.34 (blue) and 0.39 (red)); (c) \bar{u}_z (scale between -0.37 (blue) and 0.33 (red)). Velocity vector field on the cylindrical surface $\{r = 0.8\}$: (d) for $-\pi/2 \leq \theta \leq \pi/2$; (e) for $\pi/2 \leq \theta \leq 3\pi/2$. Isosurface of 10% of the velocity magnitude (purple) with streamlines (coloured by velocity magnitude): (f) from a perspective; (g) top view; the cylinder $\{r = 1\}$ is in light grey.

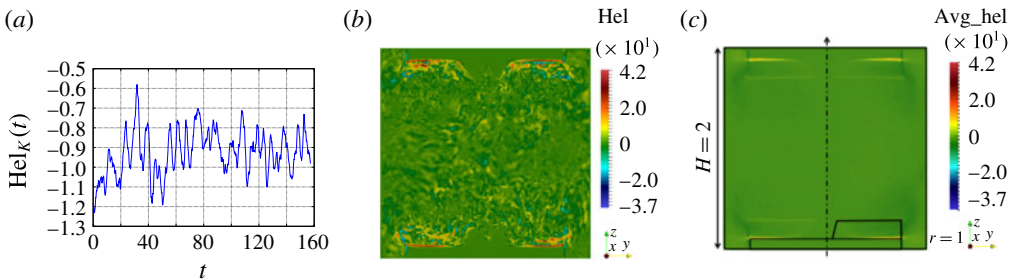


FIGURE 6. (Colour online) Navier–Stokes simulations in the TM73 VKS2 configuration at $Re = 10^5$: (a) time evolution of the total helicity $\text{Hel}_K(t)$; (b) snapshot of the helicity in the yOz plane at time $t = 125$; (c) local helicity of the time-averaged velocity in the yOz plane. The dimensions and the contour of the bottom disk and the area swept by the blades are shown in this panel.

The first quantities of interest are the kinetic energy E , the root mean square velocity and an indicator of the fluctuation level δ defined by:

$$E(t) := \frac{1}{2} \int_{\Omega} |\mathbf{u}(\mathbf{r}, t)|^2 d\Omega, \quad U_{rms} := \sqrt{\frac{2E}{|\Omega|}}, \quad \delta(\mathbf{u})(t) := \frac{\|\mathbf{u}\|_{L^2(\Omega)}^2}{\|\bar{\mathbf{u}}\|_{L^2(\Omega)}^2}. \quad (3.2a-c)$$

We also introduce the poloidal and the toroidal components of the velocity field which we denote by $P(\mathbf{u})$ and $T(\mathbf{u})$, respectively. Using the same notation and convention as in Ravelet (2005), we set:

$$P(\mathbf{u}) := \frac{1}{|\Omega|} \int_{\Omega} \sqrt{u_{r,0}^2 + u_{z,0}^2} \, d\Omega, \quad T(\mathbf{u}) := \frac{1}{|\Omega|} \int_{\Omega} |u_{\theta,0}| \, d\Omega, \quad \Gamma(\mathbf{u}) := \frac{P(\mathbf{u})}{T(\mathbf{u})}, \quad (3.3a-c)$$

where $u_{r,0}$, $u_{\theta,0}$ and $u_{z,0}$ are the radial, azimuthal and vertical components of the Fourier mode $m=0$ of the velocity \mathbf{u} . We finally consider the dimensionless torque K_p defined by:

$$K_p = \frac{1}{2} \int_{\Omega_{solid}} |(\mathbf{r} \times \mathbf{f}_s) \cdot \mathbf{e}_z| \, d\Omega, \quad (3.4)$$

where \mathbf{f}_s is the non-dimensional body force that induces the solid rotation of the impellers. Using the notation from (2.2)–(2.4), we deduce from the expression of the discrete momentum balance (2.3) that the torque at time t_{n+1} is given by

$$K_p = \frac{1}{2} \int_{\Omega} r(1 - \chi) \text{sign}(z) \frac{1}{2\tau} (4\mathbf{u}^n - \mathbf{u}^{n-1} - 3\mathbf{u}_{obs}) \cdot \mathbf{e}_{\theta} \, d\Omega, \quad (3.5)$$

with $\text{sign}(z)$ equal to 1 if $z > 0$ and -1 otherwise.

We have reported in table 2 the quantities \overline{E} , $\overline{\delta(\mathbf{u})}$, $\overline{P(\mathbf{u})}$, $\overline{T(\mathbf{u})}$, $\overline{\Gamma(\mathbf{u})}$, U_{rms} and $\overline{K_p}$ for all the runs we have done with $R_e \in \{2 \times 10^2, 5 \times 10^2, 10^3, 1.5 \times 10^3, 2.5 \times 10^3, 5 \times 10^3, 10^4, 10^5\}$. With the exception of $\overline{K_p}$ and $\overline{\delta(\mathbf{u})}$, all the quantities increase with R_e . In particular the ratio $\overline{\Gamma}$ increases with R_e and reaches the value 0.57 at $R_e = 10^5$. Using TM73 impellers, Ravelet *et al.* (2005) estimated from measurements in the bulk region $0 \leq r/R_{cyl} \leq 1$, $-0.7 \leq z/R_{cyl} \leq 0.7$ that $\overline{\Gamma} \approx 0.8$ at $R_e = 10^5$. The ratio $\overline{\Gamma}$ is expected to play a major role in the generation of a magnetic field in kinematic dynamo models using time- and azimuth-averaged velocity fields; in particular, values around 0.7 are thought to be near optimal (see figure 5 of Ravelet *et al.* (2005)) for generating magnetic fields mainly supported by the Fourier mode $m=1$ and resembling that of the kinematic dynamo discussed in § 5.1. The values of $\overline{\Gamma}$ reported in table 2 are significantly different from those reported in Ravelet *et al.* (2005). One possible origin for these differences is that we compute $\overline{\Gamma}$ whereas it is the quantity $P(\overline{\mathbf{u}})/T(\overline{\mathbf{u}})$ that is estimated in Ravelet *et al.* (2005) using 11×17 laser Doppler velocimetry measurements. Notice finally that the LES results at $R_e = 2.5 \times 10^3$ are very close to the DNS results at $R_e = 2.5 \times 10^3$ thereby confirming that, as expected, the entropy viscosity (2.11) vanishes when the flow is well resolved.

Upon inspection of figure 7, where we have reported the time-averaged torque as a function of the Reynolds number, we observe that $\overline{K_p}$ has a non-monotonic behaviour with respect to R_e . We also observe that $\overline{K_p}$ seems to be converging to a non-zero asymptotic limit when $R_e \rightarrow \infty$. Note that $\overline{\delta(\mathbf{u})}$ has the same behaviour. The behaviour of $\overline{K_p}$ and $\overline{\delta(\mathbf{u})}$ is coherent with the theoretical arguments and the experimental observations from Cortet *et al.* (2009).

In conclusion, even though our computations are performed at smaller R_e than in the experiment, the trend followed by the global quantities compares qualitatively well with the experimental results of Ravelet *et al.* (2008).

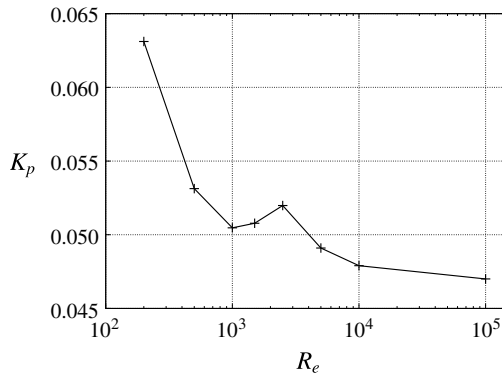


FIGURE 7. Time-averaged $\overline{K_p}$ versus R_e in log–linear showing a local maximum around $R_e = 2.5 \times 10^3$.

R_e	Model	\overline{E}	$\overline{\delta(\mathbf{u})}$	$\overline{P(\mathbf{u})}$	$\overline{T(\mathbf{u})}$	$\overline{\Gamma(\mathbf{u})}$	U_{rms}	$\overline{K_p}$
2×10^2	DNS	0.229	1.01	0.0753	0.194	0.389	0.270	0.0631
5×10^2	—	0.299	1.02	0.0933	0.201	0.465	0.308	0.0532
10^3	—	0.390	1.12	0.115	0.246	0.465	0.352	0.0505
1.5×10^3	—	0.408	1.21	0.116	0.226	0.511	0.360	0.0508
2.5×10^3	—	0.443	1.35	0.124	0.219	0.567	0.375	0.0520
2.5×10^3	LES	0.449	1.34	0.124	0.224	0.557	0.376	0.0512
5×10^3	—	0.475	1.41	0.128	0.229	0.563	0.389	0.0494
10^4	—	0.491	1.54	0.131	0.232	0.566	0.395	0.0479
10^5	—	0.519	1.49	0.134	0.235	0.571	0.406	0.0470

TABLE 2. Global quantities as defined in the text for hydrodynamic computations in the TM73 set-up.

3.3. Kinetic energy versus Reynolds number

We investigate in this section the behaviour of the kinetic energy as the kinetic Reynolds number increases.

We show in figure 8(a) the time evolution of the kinetic energy $E(t)$ for the Reynolds numbers in the range $\{2 \times 10^2, 5 \times 10^2, 10^3, 1.5 \times 10^3, 2.5 \times 10^3, 10^4, 10^5\}$. There is a unique time series since we have used the final state from the previous run as the initial condition for the next run with a higher Reynolds number. We observe that the flow is steady at $R_e = 2 \times 10^2$. It is marginally unsteady at $R_e = 5 \times 10^2$, and increasing further R_e leads to a turbulent regime. The time-averaged kinetic energy \overline{E} increases with R_e as reported in table 2.

Letting $\hat{\mathbf{u}}(r, m, z, t)$ be the m th complex Fourier component of the velocity field $\mathbf{u}(r, \theta, z, t)$, we define the kinetic energy of the m th Fourier mode by

$$E_m = \int_{\Omega_{fluid}^{2D}} \pi |\hat{\mathbf{u}}(r, m, z, t)|^2 r \, dr \, dz. \tag{3.6}$$

Figure 8(b,c) shows E_m as a function of m for $m \in \{0, \dots, 63\}$. The maximum at $m = 0$ corresponds to the large-scale forcing induced by the rotating disk. The maximum at $m = 8$ and the maxima at the corresponding harmonics are induced by the eight

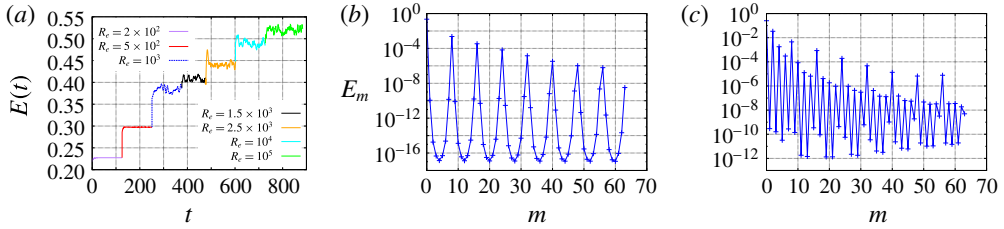


FIGURE 8. (Colour online) (a) Time evolution of the total kinetic energy $E(t)$ versus Re . Modal kinetic energy E_m as a function of the azimuthal Fourier mode: (b) $Re = 2 \times 10^2$; (c) $Re = 5 \times 10^2$.

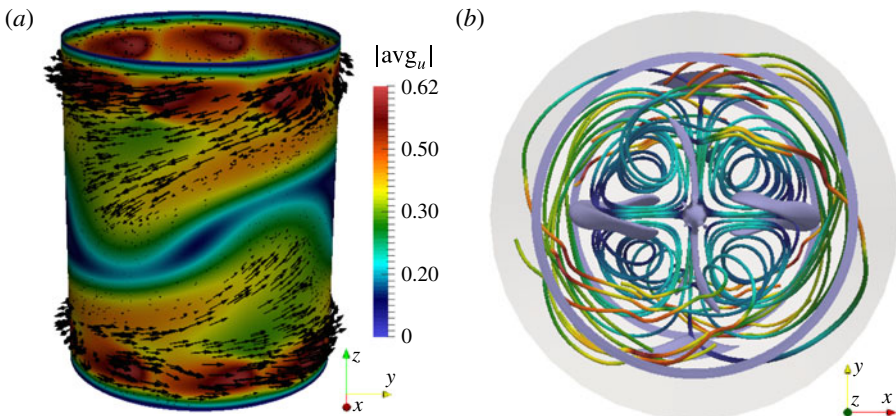


FIGURE 9. (Colour online) Navier–Stokes simulations in the TM73 VKS2 configuration at $Re = 5 \times 10^2$: (a) snapshot of the velocity vector field on a cylindrical surface at $r = 0.8$ for $-\pi/2 \leq \theta \leq \pi/2$; (b) isosurface of 6% of the maximum velocity magnitude (purple) with streamlines (coloured by velocity magnitude) from a top view; the cylinder $\{r = 1\}$ is in light grey.

rotating blades. As expected, only the Fourier mode $m = 0$ and the mode $m = 8$ together with its harmonics are populated at $Re = 2 \times 10^2$. This scenario changes when the Reynolds number is slightly increased since all the even Fourier modes are active at $Re = 5 \times 10^2$.

At $Re = 5 \times 10^2$ the flow is dominated by the Fourier modes $m = 0$ and $m = 2$ as illustrated in figure 9. Figure 9(a) shows that the azimuthal shear layer near the equator acquires a wavy structure with two co-rotating radial vortices. This phenomenon has also been observed in Ravelet *et al.* (2008). The dominance of the Fourier mode $m = 2$ and its harmonics is clearly seen when inspecting the velocity streamlines in figure 9(b). The spectrum in figure 8(b) shows that all the even modes are activated by nonlinearity.

As illustrated in figure 10, as Re increases further, the axisymmetric mode $m = 0$ and the Fourier mode $m = 8$ together with their harmonics are still energetic, but the dynamics becomes richer as the mode $m = 3$ starts to be active and eventually becomes the second largest after the axisymmetric mode (see figure 10a). This $m = 3$ structure (see figure 5) has been visualized in the experiment at very high Reynolds numbers as reported in Cortet *et al.* (2009). The structure consists of three radial co-rotating

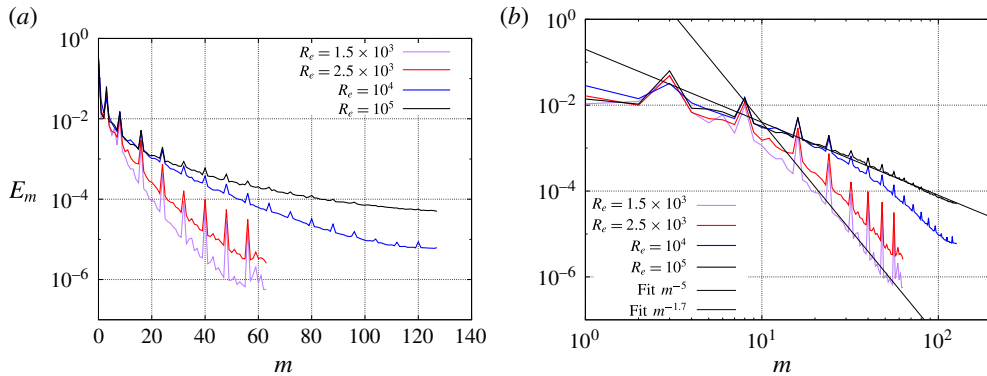


FIGURE 10. (Colour online) Spectra of the kinetic energy E_m as a function of the azimuthal mode at final time for $R_e = 1.5 \times 10^3$, 2.5×10^3 , 10^4 , 10^5 : (a) in linear-log scale, (b) in log-log scale with a fit in m^{-5} and in $m^{-1.7}$ for guiding the eye.

vortices located nearby the equatorial shear layer. The Fourier modes $m \in \{0, 3, 8\}$ and their harmonics are activated by nonlinearity as R_e grows and eventually the spectrum adopts the $m^{-5/3}$ scaling at very high Reynolds number (see figure 10). The quantity E_m decreases like a negative power of m when m is large. For instance $E_m \sim m^{-5}$ for $R_e = 1.5 \times 10^3$ and $E_m \sim m^{-1.7}$ for $R_e = 10^5$. The scaling $E_m \sim m^{-1.7}$ at $R_e = 10^5$ is close to $m^{-5/3}$ and thereby reminiscent of the Kolmogorov 1941 turbulent scaling for a one-dimensional kinetic energy spectrum (Frisch 1995).

Let us finish this section by noting that a bifurcation similar to the one discussed above, from even modes to odd modes, has been observed and reported in Herbert *et al.* (2014) at $R_e = 700$ on a configuration where the impellers are equipped with 16 blades instead of eight and the curvature of the blades is higher. Although the use of planar stereo particle velocimetry made the discrimination between odd modes like $m = 1$ and $m = 3$ uneasy, the bifurcation was attributed to a ($m = 1$) bifurcation. In this reference the authors have shown that increasing R_e from 10^2 to 10^6 leads to non-axisymmetric modulations of the axisymmetric (laminar or time-averaged) flow with successive azimuthal changes in parity (even–odd–even–odd).

4. MHD results

In this section we solve the full MHD system (2.1a)–(2.1d) using as initial velocity field a snapshot computed during the Navier–Stokes runs at the different R_e . The snapshots are selected at the end of each Navier–Stokes run when the flow is at saturation. The magnetic field $\mathbf{H} = \mathbf{B}/\mu_0\mu_r$ is initialized to a very small value which we call the seed. Unless specified otherwise, the seed is $\mathbf{H}_0 = 10^{-6}(\mathbf{e}_z + \mathbf{e}_x)$. We also add a random noise of amplitude 5×10^{-7} on all the Fourier modes $m \geq 1$ of \mathbf{H}_0 to arrive at saturation faster. We first explain how we determine the threshold for dynamo action on an illustrative case. Next we study the influence of the relative magnetic permeability of the impellers and the boundary conditions imposed on the outer boundaries of the domain $\Omega \cup \Omega_{out}$. We then fix the relative magnetic permeability of the impellers and use the pseudo-vacuum boundary conditions to investigate the variation of the critical magnetic Reynolds number with R_e .

B.C.	μ_r^{imp}	R_m^c	Dominant mode	Figure
$\mathbf{H} \times \mathbf{n} = \mathbf{0}$	1	190 ± 10	0, 1	Figure 14(a-c)
$\mathbf{H} \times \mathbf{n} = \mathbf{0}$	5	170 ± 5	0, 1	Figure 14(d,e)
$\mathbf{H} \times \mathbf{n} = \mathbf{0}$	50	90 ± 5	0	Figure 6 in Nore <i>et al.</i> (2016)
Vacuum	1	310 ± 30	1	Figures 15(a,b) and 16(a-c)
Vacuum	50	130 ± 10	0	Figures 15(c,d) and 16(d-f)

TABLE 3. Magnetic thresholds R_m^c for $R_e = 1.5 \times 10^3$. ‘ $\mathbf{H} \times \mathbf{n} = \mathbf{0}$ ’ means pseudo-vacuum boundary condition and ‘vacuum’ means that a larger integration domain with a non-conducting domain around the outer cylinder is used.

R_e	5×10^2	1.5×10^3	2.5×10^3	5.0×10^3	10^4	10^5
R_m^c	$135^* \pm 5$	$90^* \pm 5$	84 ± 5	75 ± 5	70 ± 5	70 ± 5
P_m^c	$\approx 0.27^*$	$\approx 0.06^*$	≈ 0.034	≈ 0.015	7.5×10^{-3}	7×10^{-4}

TABLE 4. Magnetic thresholds R_m^c and critical magnetic Prandtl numbers P_m^c for $\mu_r^{imp} = 50$ versus fluid Reynolds number R_e . Asterisks represent values from Nore *et al.* (2016).

4.1. Summary of our previous results

We have shown in Nore *et al.* (2016) that two distinct dynamo families compete at small Reynolds numbers (typically for $R_e < 700$) and that these two families merge at larger kinetic Reynolds numbers. In the first family, the magnetic field is essentially supported on the even Fourier modes, whereas in the second family the magnetic field is essentially supported on the odd modes; these are called the 0-family and the 1-family in Nore *et al.* (2016), respectively. In the entire section we focus on $R_e \geq 1.5 \times 10^3$; hence all the Fourier modes of the magnetic field are coupled and vary in time with the same (growth or decay) rate in the linear dynamo regime.

4.2. Dynamo threshold and saturation

In this section we fix $R_e = 10^4$ and explain how we estimate the dynamo threshold with $\mu_r^{imp} = 50$ and the pseudo-vacuum boundary condition. We are going to use the same methodology for all the other cases. The onset of dynamo action is monitored by recording the time evolution of the magnetic energy in the conducting domain, $M(t) = 1/2 \int_{\Omega \cup \Omega_{out}} \mathbf{H}(\mathbf{r}, t) \cdot \mathbf{B}(\mathbf{r}, t) \, d\mathbf{r} = 1/2 \int_{\Omega \cup \Omega_{out}} \mu_0 \mu_r |\mathbf{H}(\mathbf{r}, t)|^2 \, d\mathbf{r}$, and the modal energies $M_m(t) = \int_{\Omega^{2D} \cup \Omega_{out}^{2D}} \pi |\hat{\mathbf{H}}(r, m, z, t)|^2 r \, dr \, dz$. Linear dynamo action occurs when $M_m(t)$ increases exponentially in time (non-oscillating dynamo here) and nonlinear dynamo action takes place when $M(t)$ saturates. Various MHD runs are performed with different values of the magnetic Reynolds number R_m . The threshold for dynamo action is obtained by interpolation on the growth rate between the largest magnetic Reynolds number with a negative growth rate and the smallest magnetic Reynolds number with a positive growth rate. The interpolation is done once the bracketing interval of the threshold is small enough to yield a 5–10% error estimate. All the thresholds reported in tables 3 and 4 are accompanied with the corresponding uncertainty.

4.2.1. Linear regime

At $R_e = 10^4$ the velocity field is dominated by the Fourier modes $m = 0$ and $m = 3$ as shown in figure 10. Since the coupling term $\nabla \times (\mathbf{u} \times \mathbf{B})$ generates even magnetic

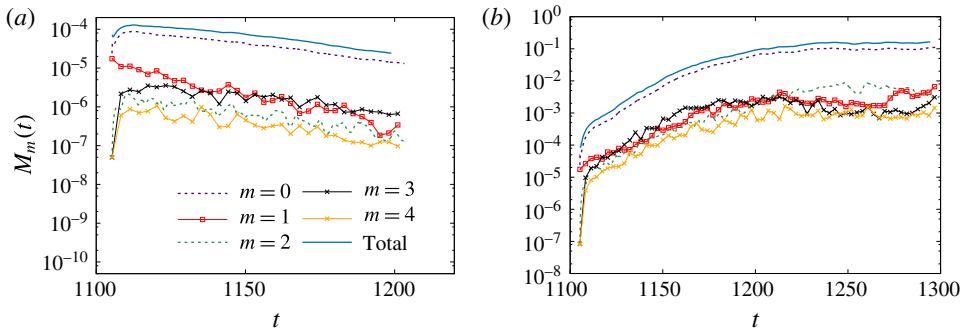


FIGURE 11. (Colour online) Time evolution of the total and modal magnetic energies $M_m(t)$ at $R_e = 10^4$ with $\mu_r^{imp} = 50$ for $m \in \{0, \dots, 4\}$: (a) $R_m = 50$; (b) $R_m = 150$.

modes from odd magnetic seeds (for example, the interaction of the seed magnetic mode $m = 1$ with the velocity mode $m = 3$ activates the magnetic modes $m = 2$ and $m = 4$, etc.) and odd magnetic modes from even magnetic seeds, all the Fourier modes of the magnetic field have the same decay or growth rate as reported in figure 11 for $R_m = 50$ and $R_m = 150$. After estimating the decay rate at $R_m = 50$ and the growth rate at $R_m = 150$, linear interpolation shows that the threshold in the considered conditions is $R_m^c = 75 \pm 5$. All the thresholds on R_m for dynamo action with $\mu_r^{imp} = 50$, the pseudo-vacuum boundary condition and $R_e \in \{2 \times 10^2, 5 \times 10^2, 10^3, 1.5 \times 10^3, 2.5 \times 10^3, 5 \times 10^3, 10^4, 10^5\}$ are reported in table 4.

We show in figure 12 the distribution of the modal energies E_m and M_m at two different times for $R_m = 150$. Note that there is dynamo action at this magnetic Reynolds number. The graphs in figure 12(a) have been done during the linear growth of the magnetic field. Those in figure 12(b) have been obtained at saturation. Note that the spectrum of the magnetic energy during the linear growth resembles that of the kinetic energy; the Fourier modes $m \in \{0, 3\}$ and the mode $m = 8$ with its harmonics are dominant.

4.2.2. Nonlinear regime

At $R_m = 150$ we have $R_m \approx 2 \times 75 = 2R_m^c$; hence the simulation done at $R_m = 150$ is far from the threshold, and the Lorentz force is therefore strong enough to retroact on the velocity field in the saturated phase. Figure 12(b) shows that the small azimuthal modes ($m \in \{0, \dots, 4\}$) of the velocity field and the magnetic field are indeed in competition at saturation ($t = 1300$); this can be seen also in figure 11(b) in the time interval $t \in [1210, 1300]$. The dominant Fourier modes of the velocity in the saturated regime are now $m \in \{0, 1, 2\}$ as seen in figure 13(a). The kinetic energy decreases while the magnetic energy increases during the time interval $t \in [1100, 1240]$ as shown in figure 13(b); at $t = 1250$ both quantities have reached asymptotic values about which they fluctuate. The retroaction of the Lorentz force makes the torque decrease by 40%; hence, quite surprisingly, driving the flow with a saturated dynamo requires less mechanical power than driving the hydrodynamic base flow (see figure 13c).

While the retroaction of the Lorentz force on the velocity field in turbulent flows has been studied in various experiments involving applied magnetic fields (see e.g. Sisan, Shew & Lathrop 2003; Miralles, Plihon & Pinton 2015), very little is known in this respect when dynamo action occurs. In the Riga experiment, an increase of approximately 10% of the power consumption has been measured at saturation,

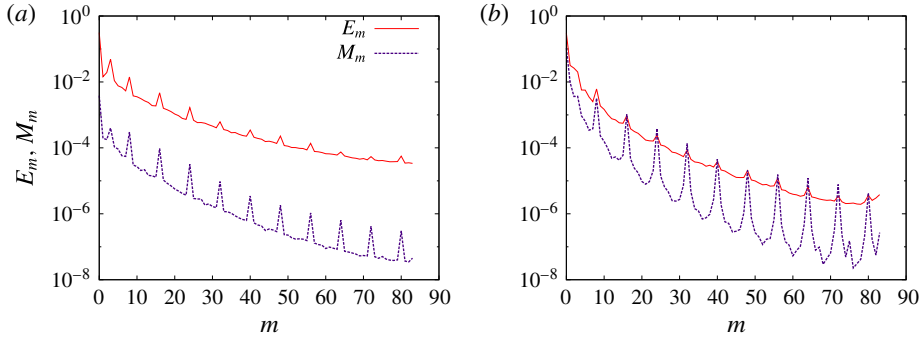


FIGURE 12. (Colour online) Spectra of the kinetic E_m and magnetic M_m energies as a function of the azimuthal mode for $R_e = 10^4$ and $R_m = 150$: (a) in the linear phase at $t = 1142$; (b) in the saturation regime at $t = 1300$.

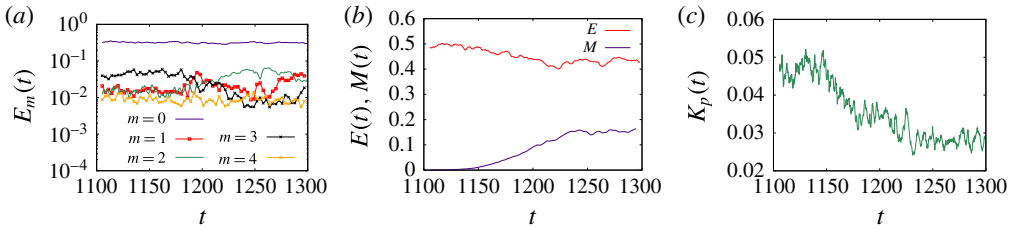


FIGURE 13. (Colour online) Time evolution of (a) the modal kinetic energies $E_m(t)$ for $m \in \{0, \dots, 4\}$ and for $R_m = 150$, $R_e = 10^4$ and $\mu_r^{mp} = 50$, (b) the kinetic and magnetic energies and (c) the total torque.

and a modification of the swirling profile together with a deceleration of the axial motion has been observed (Gailitis *et al.* 2003). In the Karlsruhe experiment, a slow down of the axial flow has been recorded in the nonlinear regime (Müller, Stieglitz & Horanyi 2004). In the VKS2 experiment, the modification of the flow in the saturation regime has been too weak to be measured. Note that the range of magnetic Reynolds numbers that can be explored experimentally is limited by the mechanical power that is available; in the above three experiments dynamo action has been investigated only in a small neighbourhood beyond the threshold.

Although very interesting, the study of the nonlinear regime over a large range of parameters is numerically expensive and therefore postponed for future work.

4.3. Impact of the magnetic permeability and boundary conditions on the threshold

We focus in this section on the influence of various parameters on the threshold and we investigate the structure of the growing magnetic field.

4.3.1. Influence of the magnetic permeability

In this section we work with the pseudo-vacuum boundary condition enforced at the outer boundary of the domain $\Omega \cup \Omega_{out}$; this boundary condition corresponds to setting $\mathbf{H} \times \mathbf{n} = \mathbf{0}$, and it is also called perfect ferromagnetic boundary condition in the literature. We also fix the Reynolds number to $R_e = 1.5 \times 10^3$. Figure 14(a–e)

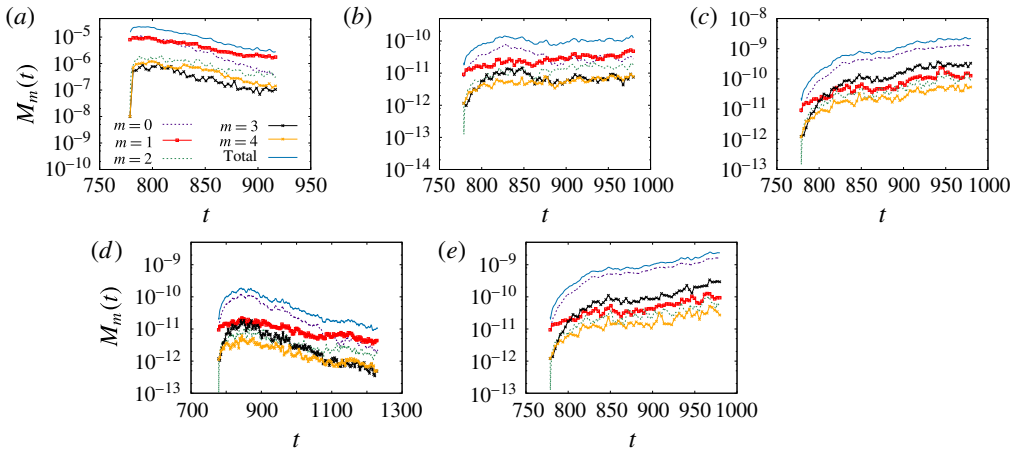


FIGURE 14. (Colour online) Time evolution of the total and modal magnetic energies $M_m(t)$ at $R_e = 1.5 \times 10^3$ with pseudo-vacuum boundary condition for $m \in \{0, \dots, 4\}$: (a–c) $R_m \in \{100, 200, 300\}$ and $\mu_r^{imp} = 1$; (d,e) $R_m \in \{150, 200\}$ and $\mu_r^{imp} = 5$.

shows the time evolution of $M_m(t)$ for the azimuthal modes $m \in \{0, \dots, 4\}$ for $\mu_r^{imp} = 1$ and $\mu_r^{imp} = 5$. The computations reported in figure 14(a) have been done with $\mathbf{H}_0 = 10^{-3}(\mathbf{e}_z + \mathbf{e}_x)$ plus a random noise of amplitude 5×10^{-5} on all the Fourier modes $m \geq 1$ of \mathbf{H}_0 as in Nore *et al.* (2016). But since it turned out that this type of perturbation was a bit too large to yield a very accurate estimate of the threshold over reasonable integration times, the other of the computations have been done with $\mathbf{H}_0 = 10^{-6}(\mathbf{e}_z + \mathbf{e}_x)$ plus a random noise of amplitude 5×10^{-7} .

When $\mu_r^{imp} = 1$ and near criticality, the behaviour of the magnetic field shows a competition between the modes $m=0$ and $m=1$ ($R_m = 100, 200$ in figures 14a,b). Well above the threshold, say at $R_m = 300$ and beyond, we recover the same dynamics as that obtained when μ_r^{imp} is larger; that is, the axisymmetric magnetic field is dominant and it is preferentially coupled to the mode $m=3$ through the velocity field. The threshold for $\mu_r^{imp} = 1$ is estimated to be $R_m^c = 190 \pm 10$. The threshold for $\mu_r^{imp} = 5$ is estimated to be $R_m^c = 170 \pm 5$. This value is slightly higher than the value $R_m^c \approx 130$ reported in Nore *et al.* (2016). The likely origin of the discrepancy is that, in order to save CPU time and to reach saturation faster, the initial seed for the magnetic field that was used in Nore *et al.* (2016) was chosen to be larger than the one presently used, and the integration time was shorter. We believe that the present estimation of R_m^c is probably more accurate. It seems finally that for small values of μ_r^{imp} , typically $\mu_r^{imp} \leq 5$, the dynamics involves interactions between Fourier modes, i.e. the unstable eigenvector is not a pure Fourier mode in azimuth, whereas the axisymmetric mode dominates when μ_r is large. Hence when μ_r is large we obtain clearer decay or growth rate, and, consequently, it is easier to estimate the threshold. The largest value of the relative permeability used in the present paper is $\mu_r^{imp} = 50$.

4.3.2. Influence of the boundary conditions

To test the influence of boundary conditions, we now enlarge the computational domain by adding an insulator around the VKS2 container (air or vacuum). The outer boundary of the computational domain is now a sphere centred at the origin and of radius 10. The magnetic field in the insulator is represented as the gradient of a scalar

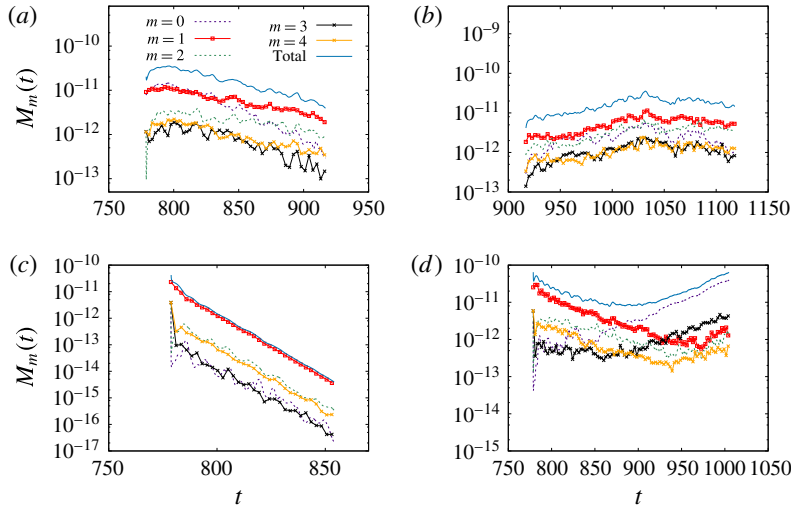


FIGURE 15. (Colour online) Time evolution of the total and modal magnetic energies $M_m(t)$ at $R_e = 1.5 \times 10^3$ with vacuum boundary condition for $m \in \{0, \dots, 4\}$: (a,b) $R_m \in \{150, 300\}$ and $\mu_r^{imp} = 1$; (c,d) $R_m \in \{50, 150\}$ and $\mu_r^{imp} = 50$.

potential as in Guermond *et al.* (2009) and this potential is enforced to be zero on the outer sphere. This configuration is a better representation of the actual experiment than that with the pseudo-vacuum boundary condition, but it is computationally more expensive.

We show in figure 15 the time evolution of the magnetic energy at $R_e = 1.5 \times 10^3$ for the Fourier modes $m \in \{0, \dots, 4\}$ with $\mu_r^{imp} = 1$ (figure 15a,b) and with $\mu_r^{imp} = 50$ (figure 15c,d). These computations have been done with the vacuum boundary condition. The seed for the magnetic field is $\mathbf{H}_0 = 10^{-6}e_x$ plus a random noise of amplitude 5×10^{-7} . We removed the axial component of the seed to demonstrate unequivocally that the axial component of the axisymmetric mode grows above the dynamo threshold. Other computations (not shown here) done with the standard seed described at the beginning of § 4 give very similar results.

For $\mu_r^{imp} = 1$, the two Fourier modes $m = 1$ and $m = 2$ compete below and above the threshold. The threshold in this case is larger than when the pseudo-vacuum boundary condition is imposed. We obtain here $R_m^c = 310 \pm 30$ whereas we had $R_m^c = 190 \pm 10$ with the pseudo-vacuum boundary condition. The increase is approximately 60%. The magnetic field is mainly supported on the Fourier modes $m = 1$ and $m = 2$ with a complex three-dimensional structure as shown on figure 16(a–c).

For $\mu_r^{imp} = 50$ the threshold is estimated to be at $R_m^c = 130 \pm 10$ (figure 15c,d). Inspection of figure 15(d) reveals that at $R_m = 150$ the Fourier mode $m = 1$ decreases in time, while the modes $m = 0$ and $m = 3$ increase and transfer energy to the other modes by nonlinear interactions for $t \geq 850$. This scenario is reminiscent of the crossing of the modes $m = 1$ and $m = 0$ discussed in Boisson & Dubrulle (2011). The present simulations show that the magnetic field is not purely axisymmetric since a significant portion of the magnetic energy is carried by the Fourier mode $m = 3$. We will examine the relative importance of the non-axisymmetric modes in § 4.5. As shown in figure 16(d–f) the growing magnetic field is mainly an axial dipole with an azimuthal component approximately even in z . The structure of a snapshot

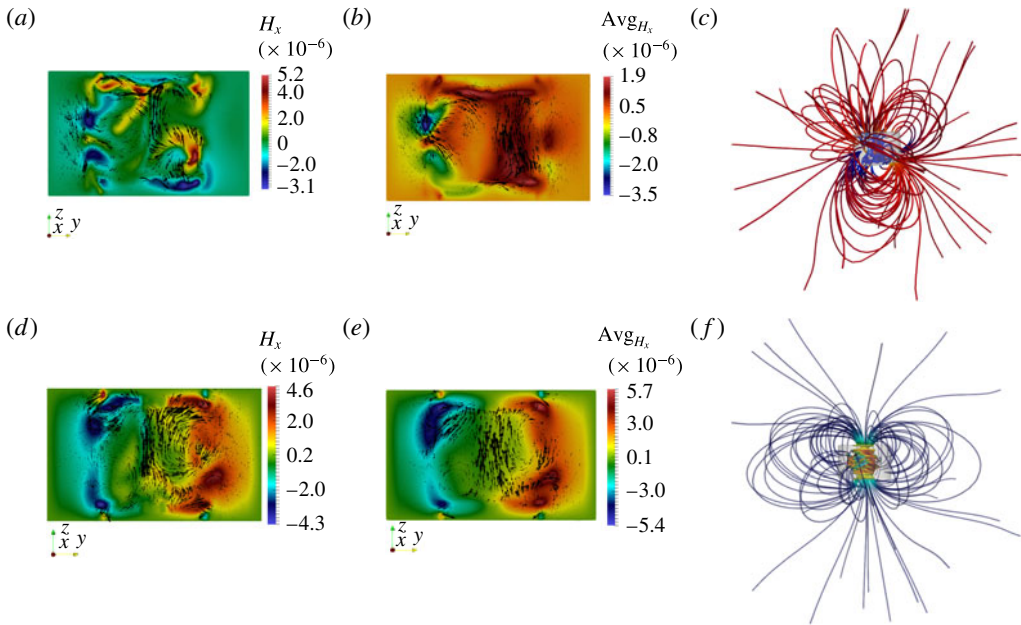


FIGURE 16. (Colour online) Magnetic field from full MHD simulations in the TM73 VKS2 configuration at $R_e = 1.5 \times 10^3$ with vacuum boundary condition: (a,b) $R_m = 300$, $\mu_r^{imp} = 1$, snapshot and time-averaged magnetic field in Ω_c ; (c) $R_m = 300$, $\mu_r^{imp} = 1$, magnetic field lines in the whole domain; (d,e) $R_m = 150$, $\mu_r^{imp} = 50$, snapshot and time-averaged magnetic field in Ω_c ; (f) $R_m = 150$, $\mu_r^{imp} = 50$, magnetic field lines in the whole domain. In (a,b,d,e) arrows represent in-plane $\{H_y, H_z\}$ vectors and colour represents the out-of-plane component H_x .

of the magnetic field (figure 16d) and the structure of the time-averaged magnetic field (figure 16e) are similar to those obtained with the pseudo-vacuum boundary condition (see figure 18a,b). This structure is also compatible with the measurements of the magnetic field made at saturation during the dynamo regime obtained in the VKS2 configuration with soft iron impellers and a copper container (see figure 6b in Boisson *et al.* (2012)).

When one compares the estimations of the threshold using $\mu_r^{imp} = 50$ and the pseudo-vacuum boundary condition, $R_m^c = 90 \pm 5$, with that obtained with $\mu_r^{imp} = 50$ and the vacuum boundary condition, $R_m^c = 130 \pm 10$, we observe a 40 % increase. This dependence of the dynamo threshold on the boundary condition is compatible with the observation made in Guermond *et al.* (2011a), Gissinger *et al.* (2008) using kinematic dynamo simulations. It is shown in these references that the perfect ferromagnetic boundary condition decreases the dynamo threshold, the minimum being achieved when this boundary condition is enforced over the entire boundary of the container. This is explained by a screening mechanism of the walls. The present full MHD simulations show the same trend.

The data collected in table 3 lead to the conclusion that using the ferromagnetic boundary condition on the external boundary of the container and using ferromagnetic material for the impeller with a large value of the magnetic permeability decreases the dynamo threshold and enhances the axisymmetric component of the magnetic field produced by the dynamo effect.

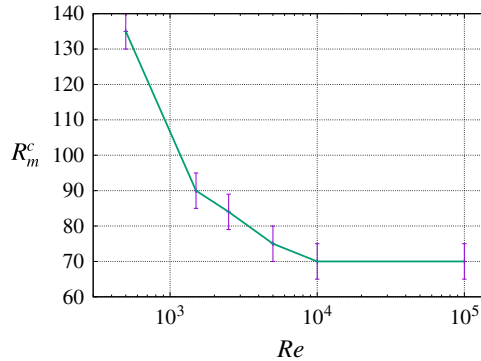


FIGURE 17. (Colour online) R_m^c versus R_e in log-linear at $\mu_r^{imp} = 50$.

A similar dominant axisymmetric magnetic field is also observed at $R_e = 2025$ and $P_m = 1/3$ for $\mu_r^{imp} \geq 12$ in Kreuzahler *et al.* (2017). In this paper, the authors study the dynamo action in the von Kármán sodium experiment for four values of the Reynolds number and three values of the magnetic Reynolds number (up to $R_e = 2025$ and $R_m = 1012.5$, using the same definitions for these control parameters as in the present article). There are similarities between the present paper and this recent reference since both works use similar penalty methods and evidence the same dominant axisymmetric dipolar magnetic field when the relative magnetic permeability of the impellers is large enough, as already pointed out by Nore *et al.* (2016). However there are two key differences between the two papers: (i) we determine thresholds over a wider range of kinetic Reynolds numbers and for larger values of relative magnetic permeability of the impellers; the largest value of the relative magnetic permeability reached in Kreuzahler *et al.* (2017) is 16, whereas we reach $\mu_r^{imp} = 50$, (this value of the relative magnetic permeability of the soft iron impellers is of the same order as that measured in the experiment, Verhille *et al.* (2010)). (ii) The penalty method in Kreuzahler *et al.* (2017) is used for the fluid part only (to confine the flow in a cylinder and to drive it with the impellers); therefore, the magnetic part is only crudely modelled, since the conductivity is assumed to be constant everywhere. This makes comparisons with the present work difficult, as we showed in table 3 that boundary conditions have a large influence on the actual values of the thresholds.

4.4. Threshold at $\mu_r^{imp} = 50$ versus R_e

We put ourselves in this section in the most favourable configuration for dynamo action to occur: we enforce the ferromagnetic boundary condition on the external boundary of the container and we use $\mu_r^{imp} = 50$. We now investigate the evolution of the critical magnetic Reynolds number as a function of the kinetic Reynolds number.

We have reported in figure 17 the estimated value of R_m^c for $R_e \in \{5 \times 10^2, 1.5 \times 10^3, 2.5 \times 10^3, 5 \times 10^3, 10^4, 10^5\}$. The critical magnetic Reynolds number seems to tend to an asymptotic value $R_{m\infty}^c$ as the kinetic Reynolds number tends to infinity. Since the kinetic Reynolds numbers associated with dynamo action in the VKS2 experiment are in the range $6.3 \times 10^6 \leq R_e \leq 8.7 \times 10^6$ (see § 2.1), figure 17 leads us to conjecture that the critical magnetic Reynolds number in this range is close to $R_{m\infty}^c$. It is indeed remarkable that the asymptotic value $R_{m\infty}^c \approx 70$ is in the range [52, 71] where dynamo action has been experimentally observed.

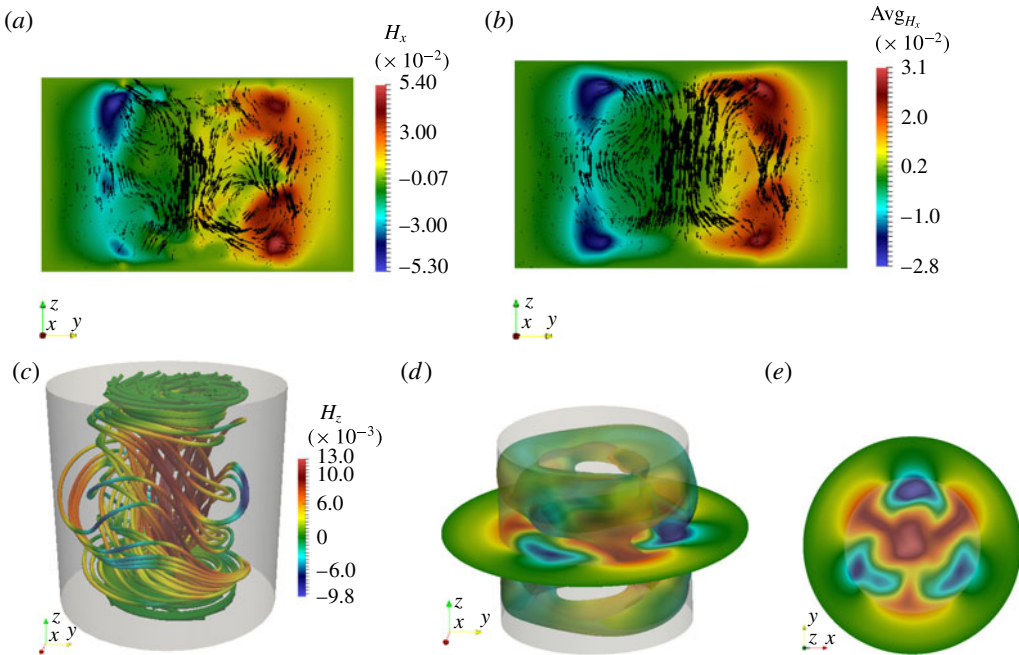


FIGURE 18. (Colour online) Magnetic field from full MHD simulations in the TM73 VKS2 configuration in the saturated regime at $R_e = 1.5 \times 10^3$, $R_m = 150$ and $\mu_r^{imp} = 50$, pseudo-vacuum boundary condition: (a,b) arrows represent in-plane $\{H_y, H_z\}$ vectors, colour represents the out-of-plane component H_x , the cylinder axis is in the middle (from Nore *et al.* (2016)). (c) Magnetic field lines of \vec{H} coloured by H_z ; (d) isosurface of 50% of the maximum amplitude of $\|\vec{H}\|$ and cut at $z=0$ for $\{r \leq 1.6\}$; (e) cut at $z=0$ from top view coloured by H_z (the inner cylinder of radius $r=1$ is indicated in light grey, the outer radius is 1.6).

Assuming, as suggested by the results reported in table 3, that going from $\mu_r^{imp} \approx 50$ to $\mu_r^{imp} = 1$ doubles the threshold for dynamo action (uniformly in R_e), it is reasonable to expect that the asymptotic limit R_m^c for $\mu_r^{imp} = 1$ is approximately $70 \times 2 \approx 140$. Hence, we conjecture that the threshold on the VKS experiment with impellers made of stainless steel might be $R_m^c \simeq 140$. The estimate of the threshold obtained experimentally by measurements of the decay time in this configuration (see Miralles *et al.* (2013): run O in figure 6, threshold reported in table 1 and R_m defined at line 24, page 8) gives $R_m^c \simeq 110$, which is in reasonable agreement with our conjectured value $R_m^c \simeq 140$ considering that the ferromagnetic walls in run O are closer to the impellers than in our computations.

4.5. Spatial structure of the magnetic field versus R_e

We continue with the pseudo-vacuum boundary conditions and $\mu_r^{imp} = 50$. Figures 18 and 19 show a snapshot of the magnetic field and the time-averaged magnetic field obtained at saturation in the dynamo regime at $R_e = 1.5 \times 10^3$ and $R_e = 10^5$, respectively. Although the time-averaged magnetic field at $R_e = 1.5 \times 10^3$ and at $R_e = 10^5$ look similar, we observe on the two snapshots in figures 18(a) and 19(a) that the magnetic field at $R_e = 10^5$ exhibits bursts near the impellers, whereas the

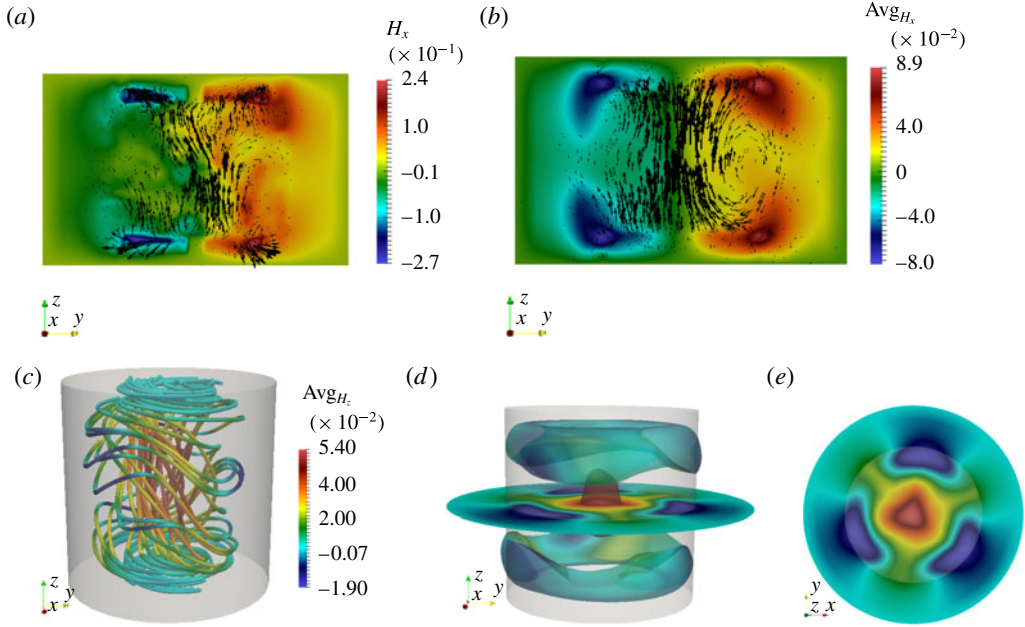


FIGURE 19. (Colour online) Same as figure 18 with $R_e = 10^5$, $R_m = 100$ and $\mu_r^{imp} = 50$. The non-dimensional geometric dimensions of the set-up are shown in (b).

magnetic field at $R_e = 1.5 \times 10^3$ is smoother. Notice also that the time-averaged magnetic vector field in the yOz plane is not strictly symmetric with respect to the Oz axis. The ratio of the magnetic energy supported by the Fourier modes $m \geq 1$ to the total magnetic energy is approximately 11% for $R_e = 1.5 \times 10^3$, $R_m = 150$ and it is approximately 18% for $R_e = 10^5$, $R_m = 100$. This little departure from axisymmetry gives a wavy shape to the magnetic field streamlines as shown in figures 18(c) and 19(c). The dominant non-axisymmetric Fourier mode of the magnetic field is $m = 3$ as shown in figures 18(d,e) and 19(d,e).

Although the flows at $R_e = 1.5 \times 10^3$ and $R_e = 10^5$ are quite different, the time-averaged magnetic fields produced by dynamo action are very similar: compare figures 18(b) and 19(b). This observation leads us to conjecture that the time-averaged magnetic field might have the same shape for the actual Reynolds number $R_e \approx 5 \times 10^6$. At least the axisymmetric shape in figures 18(b) and 19(b) is similar to the one reconstructed in figure 6(b) in Boisson *et al.* (2012). Of course, the scarcity of experimental data (Gaussmeters on a few lines) gives little information on the non-axisymmetric components.

5. Simplified models

In this section we investigate whether the mostly axisymmetric structure of the dynamo can be recovered by performing kinematic dynamo computations with flat disks and the time average of the velocity field obtained at $R_e = 10^5$ and shown in figure 5. We also take a closer look at the structure of the electrical current that is generated by dynamo action in the full MHD simulations and propose a simple interpretation of the observed dynamo.

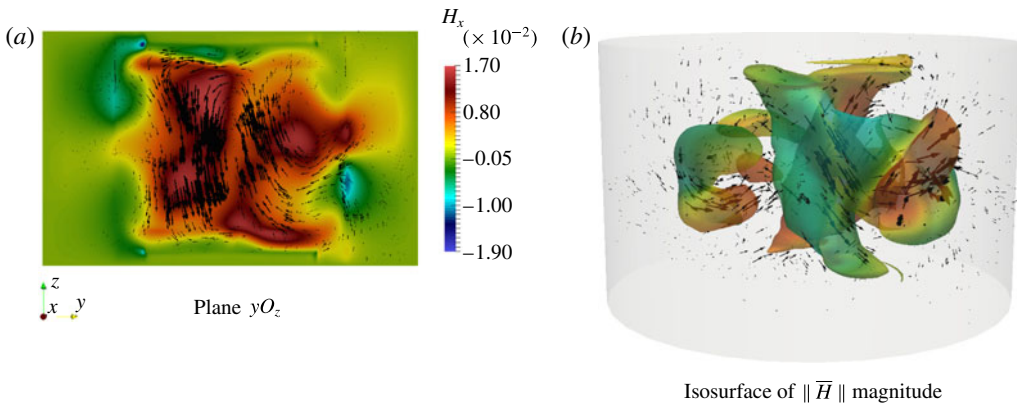


FIGURE 20. (Colour online) Magnetic field from kinematic dynamo simulations using the time-averaged velocity field at $R_e = 10^5$ with $R_m = 150$ and $\mu_r^{imp} = 50$: (a) arrows represent in-plane $\{H_y, H_z\}$ vectors, colour represents the out-of-plane component H_x , the cylinder axis is in the middle; (b) isosurface of the magnetic magnitude (coloured by the H_z component: red for upward direction and green for downward direction) at 30% of the maximum with magnetic vector fields.

5.1. Kinematic dynamo using the time-averaged velocity field at $R_e = 10^5$

A kinematic dynamo simulation is done by solving only the induction equation (2.1b) and by using the time-averaged velocity field obtained at $R_e = 10^5$; this field is shown in figure 5. The time-averaged velocity field is not axisymmetric and therefore may sustain an axisymmetric magnetic field since Cowling's theorem does not apply. We also use flat ferromagnetic disks with $\mu_r^{imp} = 50$ and we impose the boundary condition $\mathbf{H} \times \mathbf{n} = \mathbf{0}$ on the outer wall of the container.

We perform simulations with $R_m \in [50, 200]$ and find that the Fourier modes $m \in \{1, 2, 4\}$ can grow while the modes $m \in \{0, 3\}$ always decrease. The dynamo threshold is $R_m^c \approx 120 \pm 5$ and the growing magnetic field has a strong Fourier component supported on the mode $m = 1$. This unstable eigenmode has the shape of an equatorial dipole with two opposite axial structures (see figure 20). This magnetic field is similar to the one obtained in Ravelet *et al.* (2005), Guermond *et al.* (2011a) using the time- and azimuth-averaged flow measured in a von Kármán experiment done in water. In these references the amplitude of the velocity field has been multiplied by factors in the range $[0.6, 0.75]$ to test various scenarios and to make the definitions of R_e adopted in these references coincide. Once we take into account this multiplicative factor (between 0.6 and 0.75), the threshold $R_m^c \approx 120$ that we obtain is in the range of those published in the above references; for instance $43/0.75 \leq R_m^c \leq 180/0.6$ in Ravelet *et al.* (2005) and $40/0.75 \leq R_m^c \leq 82/0.6$ in Guermond *et al.* (2011a).

The main point of the present discussion is that the kinematic dynamo computation realized with the time-averaged velocity field obtained at $R_e = 10^5$ gives a dynamo that is totally different from the one obtained with the full velocity field since it is mainly supported on the Fourier mode $m = 1$. Therefore the mainly axisymmetric magnetic field shown in figure 19 cannot be attributed to the time-averaged velocity field only.

5.2. Spatial structure of the electric current versus R_e

We now focus our attention on the electric current produced by the full MHD dynamo. Figure 21(a,b) shows the electric current associated with the time-averaged magnetic

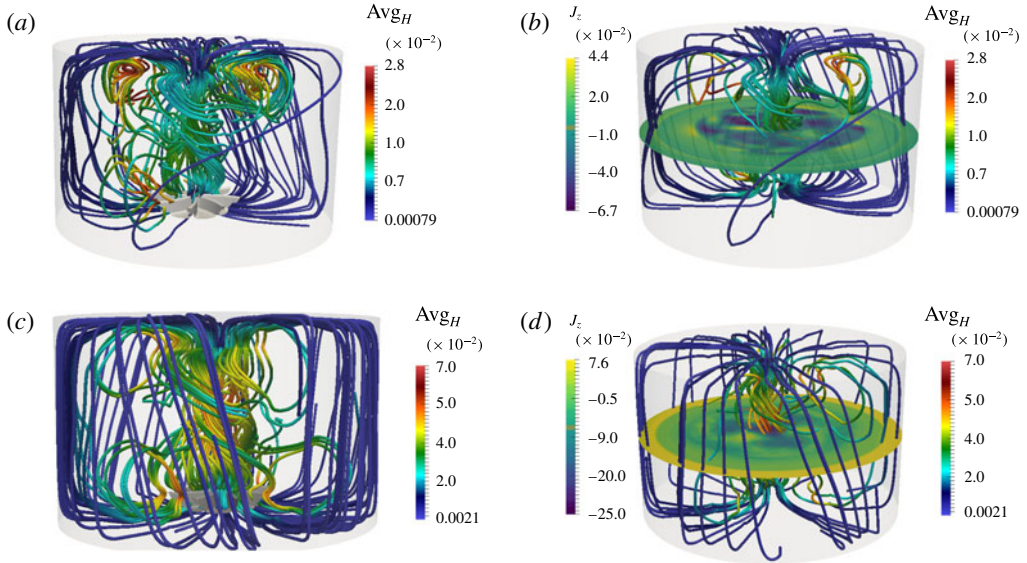


FIGURE 21. (Colour online) Electric current field from time-averaged magnetic field, $\mu_r^{imp} = 50$: (a,b) $R_e = 1.5 \times 10^3$, $R_m = 150$; (c,d) $R_e = 10^5$, $R_m = 100$; (a,c) streamlines of the current $\mathbf{j} = \nabla \times \mathbf{H}$ coloured by the magnitude of $\|\mathbf{H}\|$; (b,d) current streamlines coloured by the magnitude of $\|\mathbf{H}\|$ and slice at $\{z=0\}$ coloured by \bar{j}_z .

field computed at $R_e = 1.5 \times 10^3$ with $R_m = 150$; figure 21(c,d) shows the electric current associated with the time-averaged magnetic field computed at $R_e = 10^5$ with $R_m = 100$. In both cases we use $\mu_r^{imp} = 50$. The current distribution shows large-scale meridian loops. The current lines close to the axis have the shape of a left-handed helix going downwards; they are mainly radial in the disks (flowing outwards in the bottom disk and inwards in the top disk); they are mainly vertical and flow upwards in the copper wall (j_z is positive in figure 21(b–d) in the ring $\{1.4 \leq r \leq 1.6; z = 0\}$). The current lines also form smaller meridian loops near the blades. The poloidal component of the current ($\{j_r, j_z\}$ in the copper wall and near the blades) generates the toroidal H_θ field, while the toroidal j_θ component of the twisted helical current lines near the axis creates the axial H_z magnetic field. This organization of the current evokes the disk–dynamo of Bullard (1955) with two disks (instead of one only). The radial current in the bottom disk is collected in the copper walls, injected in the top disk, and flows from the top disk to the bottom disk in a left-handed helix. The left-hand twist of the current lines in the bulk near the cylinder axis is induced by the flow of liquid sodium. Figure 22(a) shows the current lines coloured by $\|j\|$. The current amplitude is strong near the axis. A schematic representation of the double-disk Bullard dynamo is shown in figure 22(b).

6. Summary and discussion

The main outcomes of the present paper are the following points:

- (i) The hydrodynamic computations using the entropy–viscosity-based LES technique give results in agreement with the experimental data at high Reynolds numbers. The global experimental and numerical kinetic quantities behave similarly when

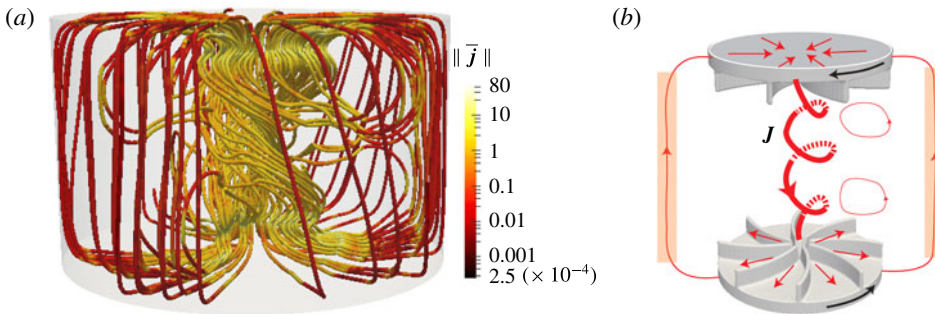


FIGURE 22. (Colour online) Current distribution: (a) current streamlines coloured by the magnitude of $\|\vec{j}\|$ (in log scale); (b) schematic of the dominant current field lines giving rise to the predominant axisymmetric time-averaged magnetic field of figure 19.

R_e increases. The modal spectrum of the kinetic energy is dominated by the azimuthal Fourier modes $m \in \{0, 2\}$ for $R_e < 700$ and $m \in \{0, 3\}$ for larger R_e . At $R_e = 10^5$, the modal spectrum behaves like $m^{-5/3}$ when m is large. In the physical space, the leading Fourier mode $m = 2$ found at $R_e = 5 \times 10^2$ corresponds to the wavy bifurcation reported in Ravelet *et al.* (2008). At larger R_e , the Fourier mode $m = 3$ is related to the three radial co-rotating vortices localized near the equatorial shear layer as observed by Cortet *et al.* (2009) in a von Kármán experiment using water.

- (ii) The full MHD computations show that, at fixed R_e , increasing the relative magnetic permeability of the impellers and/or using ferromagnetic material at the outer boundaries of $\Omega \cup \Omega_{out}$ decreases the threshold (using the pseudo-vacuum boundary condition is equivalent to adding a material with infinite permeability at the boundary). The ferromagnetic impellers enhance the axisymmetric magnetic field (Giesecke *et al.* 2012) and ferromagnetic outer walls confine the magnetic field inside the vessel. At fixed μ_r , increasing the kinetic Reynolds number also reduces the threshold. Moreover, the overall shape of the critical magnetic field averaged in time barely changes between $R_e = 1.5 \times 10^3$ and $R_e = 10^5$ as shown in figures 18 and 19. This robustness with respect to the kinetic Reynolds number may explain why the magnetic field that we computed is in very good agreement with the mainly axisymmetric magnetic field that has been experimentally observed at much higher Reynolds numbers (compare figures 18*b* and 19*b* with figure 6*b* in Boisson *et al.* (2012)).
- (iii) Using ferromagnetic boundary conditions and $\mu_r^{imp} = 50$, we have found that the critical magnetic Reynolds number tends to an asymptotic value $R_{m\infty}^c \approx 70$ when R_e increases. This value is in the range $52 \leq R_m^c \leq 71$ where dynamo action has been observed in the VKS2 set-up (see table I in Miralles *et al.* (2013)). The behaviour of R_m^c with respect to R_e that we observed suggests that the small scales of turbulence do not seem to intervene in the dynamo mechanism at high R_e numbers. This behaviour is somewhat at odd with other computations using simplistic forcings like Iskakov *et al.* (2007), Ponty *et al.* (2007), Reuter, Jenko & Forest (2011), Ponty & Plunian (2011). In all these simulations the critical magnetic Reynolds number has a non-monotonic behaviour with respect to R_e . It first increases with R_e , then either reaches a plateau or decreases after some intermediate value of R_e in the range [200, 1500]. Finally, it is suggested

in Ponty & Plunian (2011) that ‘it is the mean flow which plays the most important role in the field generation even though it is 40 % less intense than the fluctuations’. As shown in figure 10, the azimuthal Fourier modes $m \in \{0, 3\}$ of the velocity contain most of the total kinetic energy at all the kinetic Reynolds numbers we have explored (the smallest being $R_e = 500$). For instance these two modes contain about 75 % of the total kinetic energy at $R_e = 10^5$. However the kinematic computations of § 5.1 have proved that the mean flow (averaged in time but not in space, therefore with non-axisymmetric features) gives a dynamo with a magnetic field mainly supported by the Fourier mode $m = 1$ as already reported in the literature by us and others using an experimental time- and azimuth-averaged velocity field. Therefore the VKS2 dynamo cannot be attributed to the mean flow.

To conclude, our simulations at high R_e numbers confirm that the ferromagnetic impellers are crucial to reduce the dynamo threshold and to obtain the predominantly axisymmetric dynamo mode observed in the VKS2 experimental set-up. Looking at figure 22, where a schematic representation of the path followed by the electrical current is shown, the following speculative mechanism comes to mind: Let us imagine a vertical magnetic seed pointing upwards near one rotating impeller; by Ω -effect, the differential rotation of the impeller generates a toroidal magnetic field nearby the disk. This toroidal field is associated with a radial current ($j_r \approx -\partial_z H_\theta$) flowing outward in the bottom impeller and inward in the top one. The current circulates from the bottom impeller to the top one through a large-scale loop inside the copper wall. Near the axis of the vessel the current flows downwards and the current lines are twisted by the flow in a way that regenerates the initial vertical field. This is the Bullard dynamo loop (Bullard 1955) with the Ω -effect due to the disks and the twisting effect due to the flow.

Acknowledgement

The HPC resources for SFEMaNS were provided by GENCI-IDRIS (grant 2016-0254) in France and by the Texas A&M University Brazos HPC cluster. J.-L.G. acknowledges support from University Paris Sud, the National Science Foundation under grants DMS 1620058, DMS 1619892, the Air Force Office of Scientific Research, USAF, under grant/contract number FA99550-12-0358 and the Army Research Office, under grant number W911NF-15-1-0517. D.C.Q. acknowledges support by the Basque Government through ELKARTEK and the BERC 2014-2017 programmes and by Spanish Ministry of Economy and Competitiveness MINECO: BCAM Severo Ochoa excellence accreditation SEV-2013-0323. L.C. is thankful to Texas A&M University, LIMSI, and CNRS for their financial support. W. Herreman at LIMSI is greatly acknowledged for fruitful discussions and drawing figures 1 and 22(b).

REFERENCES

- BALAY, S., ABHYANKAR, S., ADAMS, M. F., BROWN, J., BRUNE, P., BUSCHELMAN, K., EIJKHOUT, V., GROPP, W. D., KAUSHIK, D., KNEPLEY, M. G., MCINNES, L. C., RUPP, K., SMITH, B. F. & ZHANG, H. 2014 PETSc users manual. *Tech. Rep.* ANL-95/11 – Revision 3.5, Argonne National Laboratory.
- BOISSON, J., AUMAITRE, S., BONNEFOY, N., BOURGOIN, M., DAVIAUD, F., DUBRULLE, B., ODIER, P., PINTON, J.-F., PLIHON, N. & VERHILLE, G. 2012 Symmetry and couplings in stationary von Kármán sodium dynamos. *New J. Phys.* **14** (1), 013044.

- BOISSON, J. & DUBRULLE, B. 2011 Three-dimensional magnetic field reconstruction in the VKS experiment through Galerkin transforms. *New J. Phys.* **13** (2), 023037.
- BONITO, A. & GUERMOND, J.-L. 2011 Approximation of the eigenvalue problem for the time harmonic Maxwell system by continuous Lagrange finite elements. *Math. Comput.* **80** (276), 1887–1910.
- BONITO, A., GUERMOND, J.-L. & LUDDENS, F. 2013 Regularity of the Maxwell equations in heterogeneous media and Lipschitz domains. *J. Math. Anal. Appl.* **408** (2), 498–512.
- BULLARD, E. C. 1955 The stability of a homopolar dynamo. *Proc. Camb. Phil. Soc.* **51**, 744–760.
- CAFFARELLI, L., KOHN, R. & NIRENBERG, L. 1982 Partial regularity of suitable weak solutions of the Navier–Stokes equations. *Commun. Pure Appl. Maths* **35** (6), 771–831.
- CASTANON QUIROZ, D. 2015 Solution of the MHD equations in the presence of non-axisymmetric conductors using the Fourier-finite element method. PhD thesis, Texas A&M College Station.
- COLGATE, S. A., BECKLEY, H., SI, J., MARTINIC, J., WESTPFAHL, D., SLUTZ, J., WESTROM, C., KLEIN, B., SCHENDEL, P., SCHARLE, C., MCKINNEY, T., GINANNI, R., BENTLEY, I., MICKEY, T., FERREL, R., LI, H., PARIEV, V. & FINN, J. 2011 High magnetic shear gain in a liquid sodium stable couette flow experiment: a prelude to an $\alpha - \Omega$ dynamo. *Phys. Rev. Lett.* **106**, 175003.
- CORTET, P.-P., DIRIBARNE, P., MONCHAUX, R., CHIFFAUDEL, A., DAVIAUD, F. & DUBRULLE, B. 2009 Normalized kinetic energy as a hydrodynamical global quantity for inhomogeneous anisotropic turbulence. *Phys. Fluids* **21** (2), 025104.
- FRICK, P., NOSKOV, V., DENISOV, S. & STEPANOV, R. 2010 Direct measurement of effective magnetic diffusivity in turbulent flow of liquid sodium. *Phys. Rev. Lett.* **105**, 184502.
- FRISCH, U. 1995 *Turbulence: the Legacy of AN Kolmogorov*. Cambridge University Press.
- GAILITIS, A., LIELAUSIS, O., DEMENT'EV, S., PLATACIS, E. & CIFERSONS, A. 2000 Detection of a flow induced magnetic field eigenmode in the Riga dynamo facility. *Phys. Rev. Lett.* **84**, 4365–4368.
- GAILITIS, A., LIELAUSIS, O., PLATACIS, E., GERBETH, G. & STEFANI, F. 2003 The Riga dynamo experiment. *Surv. Geophys.* **24** (3), 247–267.
- GIESECKE, A., NORE, C., STEFANI, F., GERBETH, G., LÉORAT, J., HERREMAN, W., LUDDENS, F. & GUERMOND, J.-L. 2012 Influence of high-permeability discs in an axisymmetric model of the Cadarache dynamo experiment. *New J. Phys.* **14** (5), 053005.
- GIESECKE, A., NORE, C., STEFANI, F., GERBETH, G., LÉORAT, J., LUDDENS, F. & GUERMOND, J.-L. 2010 Electromagnetic induction in non-uniform domains. *Geophys. Astrophys. Fluid Dyn.* **104** (5), 505–529.
- GISSINGER, C. 2009 A numerical model of the VKS experiment. *Europhys. Lett.* **87**, 39002.
- GISSINGER, C., ISKAKOV, A., FAUVE, S. & DORMY, E. 2008 Effect of magnetic boundary conditions on the dynamo threshold of von Kármán swirling flows. *Europhys. Lett.* **82**, 29001.
- GUERMOND, J.-L., LAGUERRE, R., LÉORAT, J. & NORE, C. 2007 An interior penalty Galerkin method for the MHD equations in heterogeneous domains. *J. Comput. Phys.* **221** (1), 349–369.
- GUERMOND, J.-L., LAGUERRE, R., LÉORAT, J. & NORE, C. 2009 Nonlinear magnetohydrodynamics in axisymmetric heterogeneous domains using a Fourier/finite element technique and an interior penalty method. *J. Comput. Phys.* **228**, 2739–2757.
- GUERMOND, J.-L., LÉORAT, J., LUDDENS, F., NORE, C. & RIBEIRO, A. 2011a Effects of discontinuous magnetic permeability on magnetodynamic problems. *J. Comput. Phys.* **230**, 6299–6319.
- GUERMOND, J.-L., MARRA, A. & QUARTAPELLE, L. 2006 Subgrid stabilized projection method for 2d unsteady flows at high Reynolds number. *Comput. Methods Appl. Mech. Engng* **195**, 5857–5876.
- GUERMOND, J.-L., PASQUETTI, R. & POPOV, B. 2011b Entropy viscosity method for nonlinear conservation laws. *J. Comput. Phys.* **230** (11), 4248–4267.
- GUERMOND, J.-L., PASQUETTI, R. & POPOV, B. 2011c From suitable weak solutions to entropy viscosity. *J. Sci. Comput.* **49** (1), 35–50.
- GUERMOND, J.-L. & SHEN, J. 2004 On the error estimates for the rotational pressure-correction projection methods. *Maths Comput.* **73** (248), 1719–1737; (electronic).

- HERBERT, E., CORTET, P.-P., DAVIAUD, F. & DUBRULLE, B. 2014 Eckhaus-like instability of large scale coherent structures in a fully turbulent von Kármán flow. *Phys. Fluids* **26** (1), 015103.
- ISKAKOV, A. B., SCHEKOCHIHIN, A. A., COWLEY, S. C., MCWILLIAMS, J. C. & PROCTOR, M. R. E. 2007 Numerical demonstration of fluctuation dynamo at low magnetic Prandtl numbers. *Phys. Rev. Lett.* **98**, 208501.
- KARYPIS, G. & KUMAR, V. 1998 A fast and high quality multilevel scheme for partitioning irregular graphs. *SIAM J. Sci. Comput.* **20** (1), 359–392.
- KREUZAHLER, S., PONTY, Y., PLIHON, N., HOMANN, H. & GRAUER, R. 2017 Dynamo enhancement and mode selection triggered by high magnetic permeability. *Phys. Rev. Lett.* **119**, 234501.
- KREUZAHLER, S., SCHULZ, D., HOMANN, H., PONTY, Y. & GRAUER, R. 2014 Numerical study of impeller-driven von Kármán flows via a volume penalization method. *New J. Phys.* **16** (10), 103001.
- LAGUERRE, R., NORE, C., LÉORAT, J. & GUERMOND, J.-L. 2006 Effects of conductivity jumps in the envelope of a kinematic dynamo flow. *C. R. Méc.* **334**, 593.
- LAGUERRE, R., NORE, C., RIBEIRO, A., LÉORAT, J., GUERMOND, J.-L. & PLUNIAN, F. 2008 Impact of impellers on the axisymmetric magnetic mode in the VKS2 dynamo experiment. *Phys. Rev. Lett.* **101** (10), 104501.
- MARIÉ, L., NORMAND, C. & DAVIAUD, F. 2006 Galerkin analysis of kinematic dynamos in the von Kármán geometry. *Phys. Fluids* **18**, 017102.
- MIRALLES, S., BONNEFOY, N., BOURGOIN, M., ODIER, P., PINTON, J.-F., PLIHON, N., VERHILLE, G., BOISSON, J., DAVIAUD, F. & DUBRULLE, B. 2013 Dynamo threshold detection in the von Kármán sodium experiment. *Phys. Rev. E* **88**, 013002.
- MIRALLES, S., PLIHON, N. & PINTON, J.-F. 2015 Lorentz force effects in the Bullard–von Kármán dynamo: saturation, energy balance and subcriticality. *J. Fluid Mech.* **775**, 501–523.
- MOFFATT, H. 1978 *Magnetic Field Generation in Electrically Conducting Fluids*, Cambridge Monographs on Mechanics and Applied Mathematics. Cambridge University Press.
- MONCHAUX, R., BERHANU, M., BOURGOIN, M., ODIER, P., MOULIN, M., PINTON, J.-F., VOLK, R., FAUVE, S., MORDANT, N., PÉTRÉLIS, F., CHIFFAUDEL, A., DAVIAUD, F., DUBRULLE, B., GASQUET, C., MARIÉ, L. & RAVELET, F. 2007 Generation of magnetic field by a turbulent flow of liquid sodium. *Phys. Rev. Lett.* **98**, 044502.
- MÜLLER, U., STIEGLITZ, R. & HORANYI, S. 2004 A two-scale hydromagnetic dynamo experiment. *J. Fluid Mech.* **498**, 31–71.
- NORE, C., TUCKERMAN, L. S., DAUBE, O. & XIN, S. 2003 The 1:2 mode interaction in exactly counter-rotating von Kármán swirling flow. *J. Fluid Mech.* **477**, 51–88.
- NORE, C., ZAIDI, H., BOUILLAUD, F., BOSSAVIT, A. & GUERMOND, J.-L. 2016 Approximation of the time-dependent induction equation with advection using Whitney elements: application to dynamo action. *COMPEL – Intl J. Comput. Math. Electr. Electron. Engng* **35** (1), 326–338.
- NORE, C., CASTANON QUIROZ, D., CAPPANERA, L. & GUERMOND, J.-L. 2016 Direct numerical simulation of the axial dipolar dynamo in the von Kármán sodium experiment. *Europhys. Lett.* **114** (6), 65002.
- NORNBERG, M. D., SPENCE, E. J., KENDRICK, R. D., JACOBSON, C. M. & FOREST, C. B. 2006 Measurements of the magnetic field induced by a turbulent flow of liquid metal. *Phys. Plasmas* **13** (5), 055901.
- PASQUETTI, R., BWEMBA, R. & COUSIN, L. 2008 A pseudo-penalization method for high Reynolds number unsteady flows. *Appl. Numer. Maths* **58** (7), 946–954.
- PEFFLEY, N. L., CAWTHORNE, A. B. & LATHROP, D. P. 2000 Toward a self-generating magnetic dynamo: the role of turbulence. *Phys. Rev. E* **61**, 5287–5294.
- PONTY, Y. & PLUNIAN, F. 2011 Transition from large-scale to small-scale dynamo. *Phys. Rev. Lett.* **106**, 154502.
- PONTY, Y., MININNI, P., PINTON, J.-F., POLITANO, H. & POUQUET, A. 2007 Dynamo action at low magnetic Prandtl numbers: mean flow versus fully turbulent motion. *New J. Phys.* **9**, 296.
- RAVELET, F. 2005 Bifurcations globales hydrodynamiques et magnétohydrodynamiques dans un écoulement de von Kármán turbulent. PhD thesis, Ecole Polytechnique X.

- RAVELET, F., CHIFFAUDEL, A. & DAVIAUD, F. 2008 Supercritical transition to turbulence in an inertially driven von Kármán closed flow. *J. Fluid Mech.* **601**, 339–364.
- RAVELET, F., CHIFFAUDEL, A., DAVIAUD, F. & LÉORAT, J. 2005 Towards an experimental von Kármán dynamo: numerical studies for an optimized design. *Phys. Fluids* **17**, 117104.
- RAVELET, F., DUBRULLE, B., DAVIAUD, F. & RATIÉ, P.-A. 2012 Kinematic alpha tensors and dynamo mechanisms in a von Kármán swirling flow. *Phys. Rev. Lett.* **109**, 024503.
- REUTER, K., JENKO, F. & FOREST, C. B. 2011 Turbulent magnetohydrodynamic dynamo action in a spherically bounded von Kármán flow at small magnetic Prandtl numbers. *New J. Phys.* **13** (7), 073019.
- SCHEFFER, V. 1987 Nearly one-dimensional singularities of solutions to the Navier–Stokes inequality. *Commun. Math. Phys.* **110** (4), 525–551.
- SISAN, D. R., SHEW, W. L. & LATHROP, D. P. 2003 Lorentz force effects in magneto-turbulence. *Phys. Earth Planet. Inter.* **135** (2–3), 137–159.
- STEFANI, F., XU, M., GERBETH, G., RAVELET, F., CHIFFAUDEL, A., DAVIAUD, F. & LÉORAT, J. 2006 Ambivalent effects of added layers on steady kinematic dynamos in cylindrical geometry: application to the VKS experiment. *Eur. J. Mech. (B/Fluids)* **25**, 894.
- STIEGLITZ, R. & MÜLLER, U. 2001 Experimental demonstration of a homogeneous two-scale dynamo. *Phys. Fluids* **13**, 561.
- VARELA, J., BRUN, S., DUBRULLE, B. & NORE, C. 2015 Role of boundary conditions in helicoidal flow collimation: consequences for the von Kármán sodium dynamo experiment. *Phys. Rev. E* **92**, 063015.
- VERHILLE, G., PLIHON, N., BOURGOIN, M., ODIER, P. & PINTON, J.-F. 2010 Induction in a von Kármán flow driven by ferromagnetic impellers. *New J. Phys.* **12** (3), 033006.